Accepted by ApJS

Large-Scale CO Maps of the Lupus Molecular Cloud Complex

N. F. H. Tothill[1,2], A. Löhr[1], S. C. Parshley[3], A. A. Stark[1], A. P. Lane[1], J. I. Harnett[1,4], G. A. Wright[5], C. K. Walker[6], T. L. Bourke[1] and P. C. Myers[1]

ABSTRACT

Fully-sampled degree-scale maps of the ^{13}CO 2–1 and CO 4–3 transitions towards three members of the Lupus Molecular Cloud Complex — Lupus I, III and IV — trace the column density and temperature of the molecular gas. Comparison with IR extinction maps from the c2d project requires most of the gas to have a temperature of 8–10 K. Estimates of the cloud mass from ^{13}CO emission are roughly consistent with most previous estimates, while the linewidths are higher, around 2 km s^{-1}. CO 4–3 emission is found throughout Lupus I, indicating widespread dense gas, and towards Lupus III and IV. Enhanced linewidths at the NW end and along the edge of the B 228 ridge in Lupus I, and a coherent velocity gradient across the ridge, are consistent with interaction between the molecular cloud and an expanding H I shell from the Upper-Scorpius subgroup of the Sco-Cen OB Association. Lupus III is dominated by the effects of two HAe/Be stars, and shows no sign of external influence. Slightly warmer gas around the core of Lupus IV and a low linewidth suggest heating by the Upper-Centaurus-Lupus subgroup of Sco-Cen, without the effects of an H I shell.

Subject headings: ISM: clouds — ISM: individual(Lupus) — submillimeter

[1]Harvard-Smithsonian Center for Astrophysics, 60 Garden Street, Cambridge, MA 02138

[2]School of Physics, University of Exeter, Stocker Road, Exeter, EX 4 4 QL, UK; nfht@astro.ex.ac.uk

[3]Department of Astronomy, Cornell University, Ithaca, NY 14853

[4]National Radio Astronomy Observatory, Green Bank, WV

[5]Antiope Associates, 18 Clay Street, Fair Haven, NJ 07704

[6]Steward Observatory, University of Arizona, Tucson, AZ 85721

1. Introduction

The Lupus star forming region, recently reviewed by Comerón (2008), lies about 150 pc from the Earth (Lombardi et al. 2008a), in the Gould Belt. It is immediately visible by inspection of optical photographs of the sky, comprising a set of largely filamentary dark clouds. Based on optical extinction maps (Cambrésy 1997), the 'Cores to Disks' Spitzer Legacy Programme (c2d, Evans et al. 2003, 2007, 2009), has produced and analyzed infrared images of three areas: Lupus I, III, and IV[1]. The c2d data products (Evans et al. 2007) include: Shorter-wavelength IRAC maps, used to identify and classify young stellar objects (YSOs, Merín et al. 2008); far-IR MIPS maps (Chapman et al. 2007) tracing the thermal emission of the dust component of the molecular clouds; and IR extinction maps, based on the 2MASS survey (Chapman et al. 2007) and on a combination of 2MASS and IRAC data (Evans et al. 2007). In this paper, we present maps of the c2d fields in Lupus, tracing the molecular hydrogen by the rotational emission of carbon monoxide (CO) and isotopically-substituted ^{13}CO.

The Lupus complex has been extensively surveyed in the various 1–0 transitions of CO: Murphy et al. (1986) first mapped the Lupus molecular clouds using the 1.2 m Columbia telescope with 0.5° resolution to show the extent of the molecular gas in Lupus and suggest a total mass of a few 10^4 $M_\odot$. Improved maps in several transitions were obtained by NANTEN (2.7′ resolution, but routinely undersampled): Tachihara et al. (2001) published ^{12}CO maps of the whole complex, mostly sampled at 8′ spacing, with some areas at 4′ spacing; ^{13}CO 1–0 maps (Tachihara et al. 1996) cover Lupus I and III with 8′ spacing, while C^{18}O 1–0 maps (Hara et al. 1999) cover all the clouds in the complex at 2′ spacing. Moreira & Yun (2002) mapped about 200 square arcminutes of Lupus IV at sub-arcminute resolution and full-beam spacing in the 1–0 transitions of CO, ^{13}CO and C^{18}O. The ^{13}CO 2–1 and CO 4–3 maps presented here are the first large-scale fully-sampled low-J CO maps of Lupus, and the first mid-J CO maps of any kind.

The large-scale structure of the Lupus clouds can be traced by near-IR extinction (Lombardi et al. 2008b) and CO 1–0 emission (Tachihara et al. 2001). The complex covers some 20° of galactic latitude (about 50 pc). At low latitudes ($b \lesssim 10°$), a large mass of diffuse gas contains denser filamentary clouds; at higher latitudes, the dense clouds (Lupus I and II) are more clearly separated. The evolution of the Lupus clouds may have been driven by the influence of nearby OB stars (Tachihara et al. 2001). The Lupus and Ophiuchus molecular clouds face one another across the Upper-Scorpius subgroup of the Scorpius-Centaurus OB Association; the Upper-Centaurus-Lupus subgroup lies on the opposite side of the Lupus

[1]Some authors use arabic numerals: Lupus 1, 3 and 4

clouds from Upper-Sco. The H I shell around Upper-Sco, blown by stellar winds and a presumed supernova 1.5 Myr ago (de Geus 1992), borders the NE side of the Lupus clouds; on the plane of the sky, the ridge which dominates Lupus I (B 228, see below) lies just on the trailing edge of the H I shell. The much older Upper-Cen-Lup subgroup has driven an H I shell far beyond the Lupus clouds (de Geus 1992); it should have passed through the Lupus complex some 4–7 Myr ago, roughly consistent with the ages of T Tauri stars in Lupus III and IV (Moreira & Yun 2002).

Lupus I (Fig. 1) is dominated by B 228 (Barnard 1927) or GF 19 (Schneider & Elmegreen 1979), a long ridge running NW–SE, extending over about 2° (5 pc) parallel to the edge of the Upper-Sco H I shell. The molecular material appears to fall off steeply towards the center of the shell (at the NE edge), but there is extensive material on the other side of the ridge. Lupus III (Fig. 2) is a long (about 4×1 pc) E–W cloud (GF 21, Schneider & Elmegreen 1979) at the edge of the low-latitude cloud mass: At its eastern end, it curves up to the NE and breaks up into clumps; towards the west lie two embedded (but optically-visible) Herbig Ae/Be stars, HR 5999 (A 5–7) and the B 6 HR 6000 (Comerón 2008). Tachihara et al. (2002) consider Lupus III to be a cluster-forming structure with a dense head and spread-out tail, analogous to the ρ Oph and Cha I clouds. A couple of pc north of Lupus III, there is another smaller cloud, which appears to be a separate condensation in the low-latitude gas; we henceforth refer to this northern structure as Lupus III N. Lupus IV (Fig. 3) is the head of a filamentary structure running approximately E–W (GF 17, Schneider & Elmegreen 1979; Moreira & Yun 2002), comprising a small core, about 0.5 pc long (E–W), lying within a more diffuse extended cloud, about a pc across. The filament connects Lupus IV to the low-latitude gas mass to the East; Schneider & Elmegreen describe it as a "chain of small faint globules".

Individual dark clouds or cloud peaks have been identified by inspection of optical surveys on scales ranging from degrees (e.g. B 228) to arcminutes (Sandqvist & Lindroos 1976; Feitzinger & Stüwe 1984; Hartley et al. 1986; Bourke et al. 1995a; Andreazza & Vilas-Boas 1996; Lee & Myers 1999; Vilas-Boas et al. 2000); these clouds are listed in Table 1. Near-IR extinction maps of Lupus III with resolution of 30″ (Teixeira et al. 2005) have been used to identify dark cores in more detail, which were then fitted with Bonnor-Ebert profiles. Single-pointing spectra in several molecular lines have been observed towards extinction-selected clumps: Sandqvist & Lindroos (1976) observed H_2CO along 4 lines of sight at 6 cm (6.6′ beamwidth); Bourke et al. (1995b) searched for ammonia, but did not detect it, towards two globules (BHR 120 & 140); Vilas-Boas et al. (2000) observed ^{13}CO and $C^{18}O$ 1–0, but their 0.8′ beamwidth is poorly-matched to ours; Lee et al. (2004) observed a few of their Lupus I cores (Lee & Myers 1999) in CS 3–2 and DCO^+ 2–1 (0.7′ beamwidth). Previously-identified CO cores, both those observed by Vilas-Boas et al., and those identified from their

$C^{18}O$ maps by Hara et al. (1999), are listed in Table 2. The positions of these extinction cores and $C^{18}O$ cores with respect to optical and ^{13}CO 2–1 emission are shown in Figs. 1–3. Of the members of the c2d small dark cloud sample mapped by AST/RO in ^{13}CO 2–1 and CO 4–3 (Löhr et al. 2007), three lie within the Lupus region, but outside our maps.

Lupus I contains a few YSOs, concentrated to the B 228 ridge (Merín et al. 2008). Lupus III contains a very dense cluster of YSOs near the Herbig Ae/Be stars, composed mainly of T Tauri stars (Allen et al. 2007; Merín et al. 2008), but including the Class 0 object Lupus 3 MMS (Tachihara et al. 2007). Comerón et al. (2009) identified a population of cool stars and brown dwarfs towards Lupus I and III, which are not strongly concentrated towards the molecular clouds. The Lupus IV region contains about as many YSOs as the Lupus I region (Merín et al. 2008), but they are older (Class II/III) and largely found outside the molecular cloud, with the exception of one flat-spectrum YSO candidate close to the cloud center. Even the dispersed population is absent (Comerón et al. 2009). Lupus IV thus appears to have less (or no) ongoing star formation, compared to Lupus I and III. Merín et al. suggest that the Class II and III YSOs surrounding it represent an earlier generation of star formation (possibly associated with the passage of the Upper-Cen-Lup H I shell mentioned above), and that the very dense Lupus IV core is poised to form new stars. The younger YSOs (Class 0, I and Flat-Spectrum sources from the c2d samples, Merín et al. 2008) within the boundaries of our ^{13}CO 2–1 maps are listed in Table 3, and plotted in Figs. 1–3.

2. Observations

Lupus I, III and IV were observed with the Antarctic Submillimeter Telescope and Remote Observatory (AST/RO, Stark et al. 2001), during the period 2005 March–November, in the 461 GHz CO 4–3 and 220 GHz ^{13}CO 2–1 transitions. The telescope, receiver, and spectrometer systems are described by Stark et al. (2001): ^{13}CO 2–1 observations used the 230 GHz SIS receiver, whose local oscillator system has been upgraded to use a synthesiser, frequency-multiplied ($\times$19) by a Millitech multiplier. CO 4–3 observations used the 450–495 GHz SIS waveguide receiver (Walker et al. 1992). Low-resolution acousto-optical spectrometers (1 GHz bandwidth, 0.7 MHz channel width) were used for all observations.

The large-scale maps presented in this paper were built up from multiple smaller maps ('submaps'), mosaicked together as follows: Each submap was centred on a point of a large-scale grid superimposed on the molecular cloud, the grid points separated by $24'$ and $12'$ for the 2–1 and 4–3 observations respectively. The submaps measure $28' \times 29'$ ($\alpha \times \delta$) and $12' \times 12'$ respectively, giving substantial overlap between neighbouring 2–1 maps and some

overlap (one row or column of spectra) between neighbouring 4–3 maps.

The submaps use cell sizes of $1'$ and $0.5'$, significantly oversampling the telescope beam ($3.3'$ at 220 GHz, $1.7'$ at 461 GHz). The spectra are position-switched, taken in batches of 4 or 5, all of which share a reference measurement, about a degree away. The 4 or 5 source spectra are all at the same declination (and hence at the same elevation, since AST/RO lies at the South Geographic Pole), but the reference position is the same for all spectra in a submap, and may thus differ in elevation from the source spectra by as much as a few arcminutes. The use of one reference position for each submap, however, allows the reference position to be checked for emission. Each row of each submap is built up from a number of contiguous blocks of reference-sharing spectra. Reference-sharing increases the observing efficiency almost to that of on-the-fly mapping, but also shares one of its weaknesses: The sharing of a reference spectrum produces correlated noise in neighbouring spectra, which can show up as artefacts in the map. Rather than the long stripes characteristic of on-the-fly mapping, correlated noise is manifested in the AST/RO maps as short (4- or 5-cell) horizontal blocks.

3. Data Reduction

The AST/RO observing system produces spectra calibrated onto the T_A^* scale (Stark et al. 2001); because of the unobstructed off-axis optical design of the telescope, this is essentially equivalent to T_R^*. Further reduction and processing were carried out (using COMB, the standard AST/RO data reduction program[2], and PDL[3]). The spectra have velocity resolutions of $0.9\,\mathrm{km\,s^{-1}}$ (^{13}CO 2–1) and $0.4\,\mathrm{km\,s^{-1}}$ (CO 4–3); they were checked for frequency shifts, and corrections were applied (corrections ranged from 0 to almost 5 kms — see Appendix A). Linear baselines were subtracted from all spectra, along with polynomial baselines if necessary: a few percent of the 4–3 spectra required non-linear baseline subtraction, and almost none of the 2–1 spectra (Table 4).

Long-integration spectra were taken towards all reference positions, generally showing upper limits of ~ 0.1 K (^{13}CO 2–1) and ~ 0.3 K (CO 4–3). Some 2–1 reference positions (for one submap in Lupus I and one in Lupus III) contained substantial emission (~ 1 K), and these reference spectra were added back into all the spectra in the relevant submap.

Because of the overlap between submaps, there are over a thousand pointings on the

[2]http://www.astro.umd.edu/∼mpound/comb

[3]the Perl Data Language, http://pdl.perl.org

sky towards which two or more spectra were measured at different times. These duplicate pointings can be used to estimate the internal consistency of the flux calibration at the telescope. Distributions of the ratios of peak T_R^* between spectra with the same pointings are shown in Fig. 4 for both 4–3 and 2–1 data. The typical inconsistencies between these spectra (estimated by the standard deviation of the distributions of Tr* ratios) are about 30% for CO 4–3 data, and about 20% for ^{13}CO 2–1.

3.1. Mapmaking

Initial mapmaking was carried out by nearest-neighbour-sampling the submap data onto one large grid, with overlapping observations coadded. Each pixel of these maps corresponds directly to the spectrum observed by the telescope; without smoothing, inconsistencies between neighbouring submaps show up as clear edges, which are much more obvious in the 4–3 than in the 2–1 data.

The overlap between submaps allowed these inconsistencies in the 4–3 data to be checked and corrected. Individual submaps with significantly different flux scales to their surroundings were identified and rescaled. These rescalings were checked visually: A submap was only rescaled if it was obviously higher or lower than its neighbours, if the measured scaling was consistent with the visual one, and if the rescaling improved the appearance of the map when it was applied. Rescaling corrections of $\lesssim 10\%$ did not significantly improve the appearance of the map, and were not implemented. Fewer than half the submaps needed correction, mostly by factors of 0.7–1.4 (in line with the estimate of internal consistency given above), and the largest correction factor was ~ 1.8. No corrections needed to be applied to the 2–1 data. The need to rescale probably arises from imperfect estimation of the atmospheric transparency in the calibration procedure, which works better when the atmosphere is fairly optically-thin (e.g. at 220 GHz) than at higher opacities (e.g. at 461 GHz).

The corrected 4–3 data (and uncorrected 2–1 data) were then gridded (as above) to produce final unsmoothed datacubes[4], which were used to generate the maps in this paper. All the quantities mapped are calculated directly from the data, without profile-fitting. For example, the linewidth is estimated by the ratio of integrated intensity to peak T_R^* (which overestimates the FWHM by about 10% if applied to a perfect gaussian line). Sample spectra from the datacubes are shown in Figs. 5–7.

Integrated intensity maps (Figs. 8–10), channel maps (integrated over 2 km s^{-1} channels,

[4]publicly available in FITS format at http://www.astro.ex.ac.uk/people/nfht/resources_lupus.html

Figs. 11–13), and peak T_R^* maps (Figs. 14–16) were all produced by bessel-smoothing (e.g. Jenness & Lightfoot 2000), which gives the 'most fair' representation of the sky as observed by a single-dish telescope. However, if significant emission extends to the edge of the map, this technique tends to produce a roll-off of emission in the outermost pixels of the map, and this effect is visible in some of the Lupus maps. The effective telescope diameter was picked to balance resolution against noise: 1.5 m for the 2–1 maps, and 1.2 m for the 4–3, yielding overall beamsizes of 3.8′ and 2.3′, respectively. Maps of the velocity centroid (Figs. 17–19) and linewidth (Figs. 20–22) use both unsmoothed data (in grayscale) and gaussian-smoothed data (contours), with gaussian FWHMs of 5′ (2–1) and 5.75′ (4–3) yielding overall beams of 6′ in both transitions.

The nominal pointing accuracy of AST/RO is about 1′, but comparison of the ^{13}CO 2–1 map of Lupus IV with the optical extinction structure (see Fig. 3) suggests a systematic offset in declination. Discrepancies of similar magnitude can be seen in other AST/RO data from 2005 (Löhr et al. 2007). The Lupus IV maps have therefore all been shifted southwards by 1.5′. The sub-mm map is well-correlated with the mm-wave one, and so it has been shifted as well. There is no evidence of similar systematic shifts in the Lupus I or Lupus III data. The publicly-available datacubes *do not* have this shift applied to them.

4. Results

4.1. Overview of the Lupus Clouds

Vilas-Boas et al. (2000) estimated C^{18}O 1–0 optical depths in the range 0.1–0.5 towards extinction peaks, implying that ^{13}CO 2–1 will no longer be optically-thin in dense parts of the Lupus clouds. Maps of ^{13}CO 2–1 peak T_R^* follow the extinction maps of Chapman et al. (2007) better than maps of integrated intensity do, suggesting widespread breakdown of the optically-thin approximation. The maximum peak T_R^* towards Lupus I and IV is about 3.5 K in each map, implying a minimum excitation temperature, T_x, of 8 K; the peak T_R^* in Lupus III reaches 5 K near the bright stars, so $T_x \gtrsim 10$ K in this area. Tachihara et al. (1996) adopted 13 K for their analysis of ^{13}CO 1–0 towards Lupus I. A comparison of the lower ^{13}CO contours to the most recent c2d extinction maps suggests that excitation temperatures of 8–10 K will reproduce the extinction-traced column density quite well. While higher excitation temperatures are not ruled out by the molecular line data, they would lead to lower column density estimates which would be less compatible with estimates from extinction, which is probably the least biased estimator of the true column density (Goodman et al. 2009).

Gas masses are estimated from the ^{13}CO 2–1 data as follows: The ratio of the peak

T_R^* to the maximum possible brightness temperature (for assumed T_x) yields an estimate of the peak optical depth $\tau_0^{(13)}$; this is multiplied by the linewidth to estimate $\int \tau dv$, which is proportional to the column density of ^{13}CO ($N^{(13)}$, Appendix B). $N^{(13)}$ is converted to a total gas column density by assuming conversions between $N^{(13)}$ and extinction A_V (see below), and between A_V and the column density of hydrogen ($N_{\rm H} = 1.37 \times 10^{21} A_V \,{\rm cm}^{-2}$, Evans et al. 2009). Assuming a distance of 150 pc, the total gas mass enclosed in a one-square-arcminute pixel is then calculated.

The relationship between ^{13}CO column density and extinction can be expressed as $N^{(13)} = x^{(13)} \times 10^{15}(A_V - A_{V,0})$ cm^{-2}, with the extinction threshold $A_{V,0}$ reflecting the minimum column density required for the presence of ^{13}CO. The most commonly used parameters come from a study of ρ Oph by Frerking et al. (1982, FLW): $x^{(13)} = 2.7\,{\rm cm}^{-2}$ mag^{-1}, $A_{V,0} = 1.6$ mag; other studies (e.g. Bachiller & Cernicharo 1986; Lada et al. 1994) have found values of $x^{(13)}$ in the range 2.2–2.7, and extinction thresholds of 0–1.6 mag. Recently, a comprehensive study of the Perseus complex (Pineda et al. 2008) found $x^{(13)} = 2.4\,{\rm cm}^{-2}$ mag^{-1} $A_{V,0} = 1.7$ mag overall, and $x^{(13)} = 1.9\,{\rm cm}^{-2}$ mag^{-1}, $A_{V,0} = 1.2$ mag towards the West End of the complex (PWE), comprising several dark clouds, which is likely to be the best analog to the Lupus clouds.

Estimated masses of the Lupus clouds above A_V thresholds of 2 and 3 mag are given in Table 5, along with the mean and dispersion of the linewidths of material with $A_V \geq 2$. (The linewidth distribution for $A_V \geq 3$ is very similar, varying only by about 0.1 km s^{-1}.) Masses have been calculated for $T_x = 8, 9, 10$ K and for three ^{13}CO-to-A_V relations: PWE, Perseus, and FLW. The quoted mass is the estimate using $T_x = 9$ K and PWE, and the positive and negative errors give the full range of mass estimates. Other estimates of mass and linewidth from the literature are also tabulated. Previous isotopically-substituted CO results relied, directly or indirectly, on the older ratio of N_H to A_V ($1.87 \times 10^{21}\,{\rm cm}^{-2}$, Bohlin et al. 1978), and have been rescaled to use the same ratio as in this work. The extinction mass of Lupus III has also been rescaled to assume a distance of 150 pc instead of the 200 pc used by Chapman et al. (2007) and Evans et al. (2009).

The masses of Lupus I, III (including Lupus III N) and IV are estimated to be 280, 150, and 80 $M_\odot$ respectively (for $A_V \geq 2$). The extinction mass of Lupus I (251 $M_\odot$) is similar to the ^{13}CO 2–1 estimate; those of Lupus III and IV are significantly greater (250 and 120 $M_\odot$), but still consistent with the ^{13}CO 2–1 error range. This suggests that the Lupus complex has spatial variations in the ^{13}CO-to-A_V ratio, as Perseus does (Goodman et al. 2009). By contrast, the ^{13}CO 1–0 mass estimate towards Lupus I is 880 $M_\odot$ (Tachihara et al. 1996). The ^{13}CO 1–0 map covers a much larger area than ours (almost 10 square degrees) and includes significant emission to the SE and SW of our map boundaries. Within the confines of the

^{13}CO 2–1 map, we estimate that the ^{13}CO 1–0 mass should be 600–700 $M_\odot$, still about 50% more than the upper limit of our mass range. A similar discrepancy was reported by Moreira & Yun (2002), whose mass estimate for Lupus II is about a factor of 3 lower than that of Tachihara et al.; but their mass estimate for Lupus IV is quite similar to ours. Possible reasons for the discrepancies include the undersampling of the NANTEN maps (which will tend to overestimate the area of structures) and differences in the calibration of the two telescopes. Hara et al. (1999) measured only 240 $M_\odot$ towards Lupus I in C^{18}O 1–0, which is much closer to our estimate. The additional mass in the ^{13}CO 1–0 map might comprise tenuous gas in which the 2–1 transition is not fully excited, and whose column density is low enough for it not to be detectable in C^{18}O 1–0. The ^{13}CO 1–0 mass estimate towards Lupus III (220 $M_\odot$) is consistent with our data and close to the extinction result, while the C^{18}O 1–0 estimates towards Lupus III and III N (80 and 5 $M_\odot$) are much lower.

The average linewidths for the Lupus clouds (Table 5 and Evans et al. 2009)[5] have been deconvolved by subtracting the AOS channel width in quadrature, and, at 1.5–2.7 km s^{-1}, are broader than the ^{13}CO 1–0 widths reported at emission peaks by Tachihara et al. (1996), much broader than the 0.9 km s^{-1} given by Hara et al. (1999) as the typical linewidth, and also broader than the C^{18}O 1–0 linewidths towards individual cores (Table 2). C^{18}O 1–0 is expected to display narrower lines than ^{13}CO 2–1, since the more optically-thin transition arises mainly from the denser gas in the center of the cores, which generally has a lower velocity dispersion. It is harder to see why there should be a discrepancy between ^{13}CO 1–0 and 2–1 linewidths. However, the 1–0 measurements are taken from two spectra extracted from the map, so the data are insufficient to investigate the disagreement. Despite these differences, the various linewidth measurements follow the same pattern: Lupus I and III have quite similar linewidths, Lupus III N has broader lines and Lupus IV narrower.

Based on the linewidths of ^{13}CO 2–1 and the velocity gradients observed towards the clouds, it is clear that they are gravitationally unbound (although their general filamentary shape makes the standard formula for virial mass hard to apply). Lupus IV, however, may be marginally bound due to its high column density, narrow lines and low velocity gradients: The lower limit to its virial mass is estimated to be $\sim$140 $M_\odot$, while the upper limit to the mass derived from the ^{13}CO 2–1 map is $\sim$150 $M_\odot$. Hara et al. (1999) found almost all of the dense cores that they identified in C^{18}O 1–0 to be gravitationally unbound; the greater linewidths in ^{13}CO 2–1 reinforce this conclusion.

[5]The tabulated linewidths are slightly different from those in the earlier paper: Evans et al. averaged the mean and median linewidths and took the difference between mean and median to be the error range; we only report the mean.

4.1.1. CO 4–3 emission

Because of their small areal coverage, concentrating on ^{13}CO 2–1 emission peaks, the CO 4–3 maps do not provide the same extensive overview of the clouds. The 4–3 map of Lupus I, however, covers most of the B 228 ridge. Throughout most of the ridge, the peak T_R^* lies between 1 and 2 K, corresponding to excitation temperatures of 7–9 K (assuming that the CO emission is optically-thick throughout, with a filling factor of unity). The ends of the ridge may be warmer, with peak T_R^* of 3–4 K implying excitation temperatures of 10–12 K.

The 4–3 maps of Lupus III and III N show the majority of the gas to be similar to the ridge in Lupus I, with $T_x \sim 8-10$ K. Within the main Lupus III cloud there are two maxima: one with peak T_R^* of 4 K ($T_x \sim 12$ K), while the other peaks at 9 K. This latter one appears very compact, and so its excitation temperature may be significantly higher than the 18 K minimum implied by its peak T_R^*. The 4–3 map of Lupus IV covers only the very centre of the cloud, with peak T_R^* of 3–4 K ($T_x \sim$ 10–12 K).

4.2. Lupus I

Towards the B 228 ridge, maps of extinction (Chapman et al. 2007), peak T_R^* (Fig. 14), and integrated intensity (Fig. 8) are not well-correlated. The extinction map is the most robust estimator of column density (Goodman et al. 2009): It shows a very strong peak in the middle of the ridge (DC 338.8+16.5), slightly less to the SE (339.2+16.1), and a broad low plateau to the NW (338.7+17.5). The ^{13}CO 2–1 peak T_R^* map has similar peaks towards all three dark clouds, while the CO 4–3 peak T_R^* map shows no significant peak towards 338.8+16.5 in the centre. The integrated intensity map is very different from the extinction map, with the strongest emission in the NW followed by 339.2+16.1 in the SE, and 338.8+16.5 comparatively weak in the centre (hardly appearing in the CO 4–3 integrated intensity map).

Previous molecular line studies have found a velocity gradient of about 0.3 km s^{-1} pc^{-1} along the B228 ridge (Tachihara et al. 2001; Vilas-Boas et al. 2000), but the channel and velocity maps (Figs. 11 & 17) show very little evidence of a smooth velocity gradient along the ridge. Rather, the two large clumps at the NW and SE end of the ridge have velocities that differ by about 3 km s^{-1}, while the ridge between them lies at an intermediate velocity. On the other hand, a velocity gradient across the center of the ridge shows up very clearly in both 2–1 and 4–3 maps: The gradient of about 1 km s^{-1} pc^{-1} is quite strong, compared not only to previously reported gradients in this cloud, but also to the gradients of 0.1–0.4 km s^{-1} pc^{-1} found in areas of Taurus (Murphy & Myers 1985). The gradient is smooth

and coherent over the whole of this region — an extent of more than 1 pc — and appears quite linear, which would be consistent with solid-body rotation around the long axis of the filament (Goodman et al. 1993). A coherent pattern in this region may also be seen in the linewidth maps (Fig. 20), which show an increase in linewidth towards the leading (NE) edge of the ridge. There is no sign of a velocity gradient across the NW half of B228, which suggests that the NW part of the ridge may be distinct from the center.

One of the peaks in the center of the ridge, DC 3388+165-5, is associated with IRAS 15398-3359: This Class 0 YSO (Shirley et al. 2000) has a compact ($\sim 1'$) molecular outflow with a dynamical timescale of about 2 kyr (Tachihara et al. 1996). It lies about 0.5 pc behind the steep edge of the ridge, in the E–W elongated core that forms the southern half of DC 338.8+16.5, and coincides with local maxima in integrated CO 4–3 emission (Fig. 8), in peak T_R^* of both transitions (Fig 14), and in CO 4–3 linewidth (Fig. 20).

At the SE end of the ridge, the NE spur of DC 339.2+16.1 is blueshifted from the ridge, while the rest of the clump is at about the same velocity, suggesting that the spur might be a separate cloud superposed on the ridge. Lee & Myers (1999) identified 4 optical extinction peaks in this clump: DC 3392+161-1 to -4. They associated Peak 1 with IRAS 15420–3408/HT Lup, a CTTS (Comerón 2008), which is optically visible as a nebulous patch between peaks 1, 2 and 3 in Fig 1. The other 3 'starless' peaks were observed in CS 3–2 and DCO^+ 2–1 (Lee et al. 2004): all three have $T_A^*(\mathrm{CS}) \sim 0.5$ K; DCO^+ was only detected (with $T_A^*(\mathrm{DCO^+}) \sim 0.2$ K) towards peaks 3 and 4. DCO^+ is a high-density tracer, and its presence towards peaks 3 and 4 along the ridgeline, and absence from peak 2 at the start of the NE extension, suggest that, even in this complex structure, dense gas is concentrated to the ridge. The CO 4–3 data, with better spatial and velocity resolution, show additional structure in this clump: a patch of strong emission close to DC 3392+161-4, about $10'$ across, is blueshifted by about 1 $\mathrm{km\,s^{-1}}$ with respect to the main ridge structure, leaving a cavity in the emission at ambient velocity. Molecular outflow is a possible explanation, but since there is no obvious red lobe, this would require the YSO to lie behind the cloud. Blue asymmetries in molecular lines can be caused by infall, but Lee et al. (2004) searched unsuccessfully for signs of infall towards DC 3392+161-4.

The parsec-scale ring-shaped structure to the SW of B 228 is not covered by the CO 4–3 map. However, its ^{13}CO 2–1 emission looks quite similar to that seen in the bulk of the ridge, and the detection of DCO^+ towards the dense core embedded in the SE edge of the ring suggests a significant amount of dense gas. The structure may also have a strong velocity gradient: The channel maps (Fig. 11) show two complementary semicircular structures in adjacent channels, i.e. separated by about 2 $\mathrm{km\,s^{-1}}$, equivalent to a velocity gradient of at least 1 $\mathrm{km\,s^{-1}\,pc^{-1}}$. In the linewidth map (Fig. 20), the redder NW side of the structure

has somewhat broader lines. Lee et al. (2004) observed an extinction core at the SE edge of the ring: They found no signs of infall, but both CS 3–2 and DCO^+ 2–1 are stronger in this core than in any of the cores observed in B 228. Teixeira et al. (2005) found a ring-shaped structure in extinction in Lupus III, with a diameter of about 5′, which they interpret as the remnants of the molecular cloud that formed the nearby cluster of young stars. By contrast, this structure is larger (20′) and is not associated with a known cluster.

4.3. Lupus III

CO emission towards Lupus III in both transitions is dominated by a compact source in the West of the cloud, close to core F identified by Teixeira et al. (2005). Proceeding from E to W are: Core F; the compact CO source (slightly blueshifted from the bulk of the cloud); the HAe/Be stars HR 5999 and 6000; and further ^{13}CO 2–1 emission extending E–W. This latter emission shows no particular sign of the ring structure found in extinction by Teixeira et al. (2005), probably because the central void is smaller than the 220 GHz beam. There is a significant velocity gradient across this area, of about 2 $\mathrm{km\,s^{-1}\,pc^{-1}}$, getting redder to the west, which is not simply due to the blueshifted emission of the compact source to the east.

To the east of the compact source, extinction cores A–E (Teixeira et al. 2005) blend together at this resolution: The integrated intensity map (Fig 9) shows two E–W spurs off the emission peak, the northern containing cores C and D, and the southern containing E. Further east still, the northern spur continues to core B, while A lies just NE of DC 3397+92-3. The strongest $H^{13}CO^+$ emission in this area ($\sim$ 1 $\mathrm{K\,km\,s^{-1}}$) is found towards Core E; Core D, with about half the $H^{13}CO^+$ emission, contains the Class 0 YSO Lupus 3 MMS (Tachihara et al. 2007).

Lupus III N, the small ($<$ 0.5 pc) cloud core lying a few pc N of Lupus III, shows surprisingly complex structure: ^{13}CO 2–1 channel and velocity maps (Figs. 12 & 18) show the core to be lying in a larger ($\sim 2 \times 1$ pc) structure, elongated SE–NW, with a significant velocity change over the long axis. The velocity gradient is dominated by a sudden change just SE of the cloud core, also seen as a sharp edge in the reddest 2–1 channel map.

4.4. Lupus IV

The E–W elongated core of Lupus IV has 3 peaks along its length: The central and western ones correspond to the extinction peak which reaches $A_V \sim 24$ mag. The peaks are most obvious in the ^{13}CO 2–1 channel maps (Fig. 13); the peak T_R^* map (Fig. 16) shows

them with much lower contrast than the extinction maps as the ^{13}CO transition is optically-thick ($A_V \sim 24$ mag corresponds to $\tau_0^{(13)} \sim 8$–10). Moreira & Yun (2002) found the ^{13}CO 1–0 line to be optically thick as well, saturating with respect to 100 μm IR emission. The eastern peak has broader lines yielding similar integrated intensity (Fig. 10); at finer velocity resolution, these lines are found to be double-peaked (Moreira & Yun 2002). Although there is quite strong CO 4–3 emission throughout the core, and the velocity structure of the 4–3 emission is similar to that of ^{13}CO 2–1, the integrated 4–3 emission is concentrated towards the E and W condensations only. Two elongated structures running NE of the core are also visible in the CO 4–3 peak T_R^* map.

The strong velocity gradients seen in Lupus I and III are absent from Lupus IV. Some velocity structure is evident: The central condensation in the core and the two elongated NE structures are blueshifted (by 1–2 km s^{-1}) compared to the E and W condensations. Moreira & Yun (2002) reported significant velocity structure in the E–W direction, but our velocity maps show that this E–W structure is not found throughout the cloud.

4.5. Comparison of CO transitions

4.5.1. Whole clouds

CO 4–3 emission from the Lupus clouds can be compared to that of ^{13}CO 2–1 by gaussian-smoothing the CO 4–3 map and plotting the integrated intensities (Fig. 23) and peak T_R^* (Fig. 24) against one another, point-by-point. The peak T_R^* comparison is noisier than that of integrated intensity, and is only shown for Lupus I and III, which have stronger emission.

The large 4–3 map of Lupus I provides an overview of the bulk of the molecular gas. Clusters of points close to the origins of the integrated intensity and peak T_R^* plots reflect the noise levels in the maps. The majority of the data are somewhat correlated, occupying regions of the plots bounded by (4–3)/(2–1)$\gtrsim 0.5$ (both plots), $\int T_R^*(4-3)dv \lesssim 6\,\mathrm{K\,km\,s^{-1}}$(integrated intensity), and $T_R^*(4-3) \lesssim 2.5\,\mathrm{K}$ (peak). The 4–3 emission is effectively saturated, while the ^{13}CO 2–1 emission takes a wide range of values. This suggests that even regions of quite low column density contain sufficient dense gas to emit optically-thick CO 4–3 radiation (the critical density of CO 4–3 is of order $10^4\,\mathrm{cm^{-3}}$, but see Sec. 5.1).

Another population of molecular gas can be identified towards Lupus I: Its ^{13}CO 2–1 peak T_R^* is similar to that of the bulk population, while its CO 4–3 peak T_R^* is greater ($T_R^*(4-3) \lesssim 4\,\mathrm{K}$). This suggests that the gas is warmer, but not denser than the bulk of the cloud. The integrated intensities of the transitions, however, are well-correlated;

this probably arises from increased linewidths in both transitions, and thus from increased velocity dispersion in the gas. Inspection of the maps of integrated intensity, peak T_R^* and linewidth towards Lupus I (Figs. 8, 14, 20) shows that this component, with enhanced integrated intensity, peak CO 4–3 T_R^* and linewidth, is found in the NW end of B 228.

The much smaller CO 4–3 maps towards Lupus III, III N, and IV provide fewer data. However, two components can still be identified in Lupus III: one component consistent with the Lupus I bulk population, and the other with stronger emission. In contrast to its counterpart in Lupus I, both integrated intensity and peak T_R^* of the brighter component are well-correlated. This brighter component consitutes the compact peak close to the HAe/Be stars in Lupus III. Heating by the nearby stars could increase the peak T_R^* and hence the integrated intensities of both transitions, without a significant change in the linewidth. The molecular gas in Lupus III N and IV occupies a similar region of the integrated intensity plot to the bulk population of Lupus I, suggesting broadly similar physical conditions.

Some positions show significant CO 4–3 emission without ^{13}CO 2–1: The spectra towards one of these positions are shown in Fig. 5, and the integrated intensity and peak T_R^* plots show that this occurs in all the clouds. The combination of strong CO 4–3 emission and weak or absent ^{13}CO 2–1 implies warm gas with low column density; since the CO 4–3 map areas were chosen to cover ^{13}CO 2–1 peaks, there may be more of this population outside our 4–3 maps.

4.5.2. Dense cores

Spectra towards specific cores have been measured by NANTEN and SEST: Hara et al. (1999) list the C^{18}O 1–0 line parameters for the spectrum at the peak of each dense core identified from their map, and Vilas-Boas et al. (2000) list parameters for both ^{13}CO and C^{18}O transitions towards extinction-selected cores. Because the AST/RO maps are fully-sampled, it is possible to obtain equivalent spectra (albeit with a beamwidth of 3.3′, compared to the 2.8′ NANTEN beam, and SEST's 0.8′ beam) and compare the peak T_R^* (Fig. 25) and integrated intensities (Fig. 26).

The peak T_R^* in CO 4–3 and ^{13}CO 2–1 towards most of the cores lie in the same region of the plot as the bulk component of molecular gas described above. Four cores are clearly brighter than the rest: The two identified in Lupus III are both associated with the bright compact source, the one in Lupus I lies at the SE end of B 228, and the one in Lupus IV is in the middle of the central core. The majority of the extinction cores have ^{13}CO 2–1/1–0 peak T_R^* ratios in the range 0.3–0.7, inconsistent with the 0.7–2 expected from LTE

(Appendix B). This could be caused by beam-dilution compared to the sub-arcminute SEST beam (but see below). The exception (one of the Lupus III cores associated with the bright compact source) has a T_R^* ratio of almost 3: It may be large enough not to suffer beam dilution, and warm enough to be close to the high-temperature line ratio limit. While the Lupus I and III cores are well-mixed in the plot, the Lupus IV cores have rather low line ratios. There is no particular reason for them to be more beam-diluted, so the lower line ratio may reflect a lower temperature. The plot of ^{13}CO 2–1 peak T_R^* against that of C^{18}O 1–0 does not show any clear separation between the extinction and C^{18}O core samples. This is surprising, since the C^{18}O cores observed by NANTEN should suffer almost as much beam dilution as the AST/RO data, compared to the extinction-selected cores observed by SEST. The line ratios of the cores lie mainly between unity and ~ 3; correcting for the factor-of-2 T_R^* discrepancy estimated above, this suggests line ratios of about 2 to 6, in line with LTE estimates for C^{18}O optical depths of 0.1–0.5 (Vilas-Boas et al. 2000).

The CO 4–3 and ^{13}CO 2–1 integrated intensities of the cores are more scattered, but the high-T_R^* cores in Lupus III also have the highest integrated intensities. In contrast, the high-T_R^* cores in Lupus I and IV have more average integrated intensity, suggesting that the increased T_R^* (and hence temperature and/or density) is not accompanied by increased linewidth. The two more cores in Lupus I with large ^{13}CO 2–1 integrated intensity also lie in the SE of B 228. The ratios of the two ^{13}CO transitions (2–1/1–0, for the extinction-selected cores only) lie between about 0.7 and 1.5 (with a few between 1.5 and 3), which is consistent with our expectations from LTE, but not with the peak T_R^* ratios above. Line parameters were estimated from the SEST data by fitting gaussian line profiles (Vilas-Boas et al. 2000), in contrast to the AST/RO and NANTEN data, for which integrated intensity and peak T_R^* were measured directly, and the linewidth estimated by the ratio. This difference in analysis could cause a systematic discrepancy, with the SEST analysis yielding lower T_R^* and broader linewidths. The cores with higher ratios (1.5–3) are all in Lupus I or III, but are scattered throughout the clouds. Ratios of ^{13}CO 2–1 to C^{18}O 1–0 integrated intensity are around 3–6 for the C^{18}O-selected cores observed with NANTEN (consistent with the peak T_R^* ratios above), but the same ratios towards extinction cores are generally higher. These high ratios generally arise from rather low C^{18}O 1–0 integrated intensities ($\lesssim 0.5$ K km s^{-1}).

4.6. CO Emission towards YSOs

The YSO population of Lupus is dominated by Class II and III objects (Comerón 2008; Merín et al. 2008), but younger objects are also found there. The Class 0/I/F sources identified by Merín et al. lying within the ^{13}CO 2–1 maps are listed in Table 3, together

with the 2–1 line parameters towards them and, where applicable, CO 4–3 parameters; two objects that have been identified as background galaxies (Comerón et al. 2009) are excluded. Spectra towards the YSOs are shown in Figure 27: All 2–1 spectra are pointed within 0.6′ of the YSO position, and all 4–3 spectra are within 0.25′. Spectra towards some YSOs do not show any significant emission: Values of T_R^* below $\sim$ 1K (in either transition) should be treated as noise.

Of the 4 YSOs in Lupus III with very low or non-existent 2–1 emission, Comerón et al. (2009) estimate 3 to have ages of order 100 Myr. The rest of the YSOs have linewidths similar to those of the surrounding molecular gas. This does not rule out the presence of line wings due to outflow: The Class 0 source Lupus 3 MMS has quite average linewidths in both transitions, but the spectra themselves clearly show wings. The flat-spectrum source J154506.3–341738 (in Lupus I) has broader-than-average lines; nebulosity prevented it from being measured in the optical by Comerón.

5. Discussion

5.1. The Bulk Molecular Material

The estimates of column density, and hence mass, derived above assumed a blanket temperature of 9 ± 1 K rather than the 13 K assumed by Tachihara et al. (1996) for Lupus I and the 12–17 K estimated towards Lupus IV by Moreira & Yun (2002), both based on optically-thick CO 1–0 emission. 8 K is the minimum excitation temperature consistent with the peak ^{13}CO 2–1 T_R^* seen towards the majority of the gas in Lupus I, III and IV, and with the peak CO 4–3 T_R^* over most of the B 228 ridge. Adopting excitation temperatures close to the minimum implies assumptions of optical thickness, LTE, and a filling factor close to unity, but is required for consistency with the extinction maps (Evans et al. 2007): The $A_v = 2.5$ and $T_R^*(^{13}\mathrm{CO}\ 2\text{–}1) = 1.5$ K contours are quite similar. This implies $T_x \lesssim 10$ K for both PWE and FLW ^{13}CO-to-A_V relations, although it does allow a higher T_x towards Lupus I for the Perseus ^{13}CO-to-A_V parameters.

The gas temperature estimate is consistent with estimates for many dark clouds. Vilas-Boas et al. (2000), using ^{13}CO and C^{18}O 1–0 transitions, estimated the excitation temperatures of their sample of dense cores in Lupus to lie in the range 7–15 K, with the majority of good estimates being colder than 10 K; Clemens et al. (1991) estimated gas temperatures towards a large sample of small dark clouds from CO 2–1, and found that the majority were colder than 10 K. Models of cold dark clouds yield dust temperatures <10 K at the centre (Evans et al. 2001; Zucconi et al. 2001). While the dust temperature is higher towards the

cloud surface, gas temperatures are lower than dust temperatures for low column and volume densities (e.g. Doty & Neufeld 1997), so the ^{13}CO 2–1 and CO 4–3 transitions need not be dominated by the cloud centres. The CO 1–0 estimates mentioned above are likely to be dominated by the cloud surfaces, which may be warmer than those of the majority of dark clouds due to external heating by the nearby OB association. The peak CO 4–3 T_R^* towards Lupus IV implies a T_x of 10–12 K, compared to $T_x \sim 8$ K from ^{13}CO 2–1. This may reflect a combination of external heating, as suggested by Moreira & Yun (2002), with high enough density to couple the gas and dust temperatures more effectively than in Lupus I or III.

The column density of H_2 throughout most of the B 228 ridge is within a factor of 2 of 5×10^{21} cm^{-2}(Chapman et al. 2007). The width of the ridge on the sky is about 10′, or 0.4 pc; if B 228 is assumed to be a filamentary cloud, with a similar depth, the average volume density $\overline{n}$ is a few 10^3 cm^{-3}. This is close to the critical density n_c of the 2–1 transitions of CO and its isotopologues, supporting the assumption of LTE used throughout this work, but an order of magnitude lower than the critical density of CO 4–3 (a few 10^4 cm^{-3}, Appendix B). Evans (1999) found that significant emission in many transitions could arise from gas with volume density more than an order of magnitude lower than n_c (although CO was not included in that study), but the similarity between the excitation temperatures of ^{13}CO 2–1 and CO 4–3 suggests thermalised emission, and thus a volume density close to n_c. The line emission is pervasive, which argues against its arising from cores or a high-density centre of the ridge. However, if the bulk of the ridge material were taken to be close to the critical density of CO 4–3, the depth of the ridge along the line of sight would be an order of magnitude lower than its width in the plane of the sky, which seems implausible. It is more likely that the CO 4–3 emission arises from a small fraction of dense gas found in clumps throughout the molecular cloud; or from a thin warm shell around the outside of the cloud; or that subthermal emission from the bulk of the molecular gas can account for the CO 4–3 lines seen throughout the cloud. The latter possibility, in particular, may be checked by modelling the emission.

5.2. Cloud Cores

Vilas-Boas et al. (2000) estimated the optical depth of C^{18}O 1–0 towards their dark cloud sample to lie in the range 0.1–0.5 by comparing the ^{13}CO and C^{18}O lines, and assuming an abundance ratio of 5.5. A large fraction of their cores had line ratios in excess of 5.5, inconsistent with their assumed isotopologue ratio; however, ratios up to 8 are possible (Appendix B). Hara et al. (1999) estimated somewhat lower optical depths towards their C^{18}O cores, assuming $T_x = 13$ K; at $T_x = 9$ K, their estimated optical depth range becomes

quite consistent with that of Vilas-Boas et al.. The ^{13}CO 1–0 optical depth towards the cloud cores is likely to range from 0.5 up to 2–4, depending on the abundance ratio.

Teixeira et al. (2005) estimated volume densities of a few 10^4 cm^{-3} for the dense cores they identified in Lupus III. If such densities are widespread among the dense cores in Lupus, the CO 4–3 transition is close to LTE, and it becomes possible to estimate the expected value of $(T_R^*)_{4-3}/(T_R^*)_{2-1}$ towards the cores. At $T_x = 9\,\mathrm{K}$, the high-column-density limit of the ratio (both transitions optically-thick) is ∼0.4; as the optical depth of ^{13}CO becomes moderate, the ratio increases towards unity. However, at low optical depths, CO 4–3 may no longer be thermalised, making this estimate invalid. Most of the cloud cores have 4–3/2–1 ratios clustered around 0.5 (Fig. 25), with a few more at unity or above, and one over 1.5. It is difficult to achieve a line ratio significantly above unity under LTE: Even at low optical depth, the temperature would need to be at least 20 K.

5.3. Lupus I

The central condensation in the B 228 ridge (338.8+16.5) has high extinction, moderate peak and integrated T_R^* in ^{13}CO 2–1, and CO 4–3 emission quite similar to the bulk of the cloud. The linewidth is also quite similar to that of the bulk cloud, so the enhancement in ^{13}CO 2–1 is largely due to the increased peak T_R^*. Elevated gas temperature would likely show up in the CO 4–3 emission, so the increased T_R^* is largely due to the increased column density as the ^{13}CO 2–1 transition becomes optically-thick. This dense cloud seems to have more in common with the bulk material around it than it does with the emission peak to the NW, having similar temperature and linewidth. It is also associated with two embedded YSOs, including a known outflow source.

The strong, coherent velocity gradient seen north and east of 338.8+16.5 runs perpendicular to the leading edge of the ridge (i.e. in the direction of the H I shell's expansion); the leading edge (i.e. towards the centre of the shell) has a greater linewidth than the gas behind it. It is difficult to rule out temperature and optical-depth effects combining to mimic a velocity gradient, but similar patterns are seen in both ^{13}CO 2–1 and CO 4–3 maps: A truly optically-thin tracer is required to confirm the gradient. If the apparent gradient truly reflects the kinematics of the gas, the total change in velocity across the ridge is about $1\,\mathrm{km\,s^{-1}}$, or half the linewidth. However, the change in velocity across a Jeans length (around 0.1 pc for these clouds) is only about $0.1\,\mathrm{km\,s^{-1}}$, which is unlikely to add significant support against collapse. Indeed, 338.8+16.5 seems to be part of this velocity field, and contains a known Class 0 YSO.

The integrated intensity maximum at the NW end of B 228 is due to the combination of enhanced peak T_R^* and broader lines. Throughout this area, the peak CO 4–3 T_R^* is $\gtrsim 3\,\mathrm{K}$, implying a gas temperature of at least 10 K. Although the 4–3 emission probably does not sample the whole of the gas column, there is supporting evidence for a warmer temperature: The Spitzer IR maps (Chapman et al. 2007) show this end of the filament to be bluer than the central part, with strong 24 μm emission (see also Merín et al. 2008), which could be due to a higher dust temperature. No Class 0/I/F YSOs are found in the northern part of the ridge, and only one Class III (Chapman et al. 2007), so there are no obvious internal heating sources. The nearby Upper-Sco OB subgroup lies to the NE of Lupus I, but is unlikely to be causing the heating, since no similar effect is to be found in the centre of the ridge.

At the SE end, the picture is complex: The extinction and peak T_R^* for both transitions are high at the SE end of 339.2+16.1, while linewidth and integrated intensity peak further NW. The strong enhancement of peak CO 4–3 T_R^* at the SE end suggests increased temperature as well as column density. The associated YSOs all lie to the NW in this area, so internal heating seems unlikely.

5.3.1. Interaction with the Upper-Sco shell

The H I emission from the Upper-Sco shell lies at a similar velocity (3–9 $\mathrm{km\,s^{-1}}$, de Geus 1992) to the Lupus clouds, consistent with their being in contact with one another, and Lupus I being dynamically affected by the shell. If such an interaction is going on, the combination of continuity and conservation of momentum require that the sum of pressure and momentum flux is conserved by the interaction. The limitations of both molecular and atomic data make it impossible to look for clear diagnostics of interaction between the shell and ridge, but some rough estimates can be made. For both phases,

$$\frac{\left(P+\rho v^2\right)/k}{\mathrm{cm^{-3}K}} = \mu\left(\frac{n}{\mathrm{cm^{-3}}}\right)\left(\left(\frac{\sigma_v}{\mathrm{kms^{-1}}}\right)^2+\left(\frac{v}{\mathrm{kms^{-1}}}\right)^2\right)$$

where $\mu = 170$ for H I, and 340 for H_2. Based on the H I data (de Geus 1992), this quantity may be estimated to be of order $10^6\,\mathrm{cm^{-3}K}$, about 90% of which is the momentum flux component due to the expansion velocity of the shell ($10\,\mathrm{km\,s^{-1}}$, de Geus 1992). $P+\rho v$ for the molecular gas in Lupus I is also around $10^6\,\mathrm{cm^{-3}K}$, but is approximately evenly divided between pressure and momentum flux (due to velocity gradients).

The rough similarity in this sum between the H I and molecular gas is consistent with interaction between them. If the H I shell is indeed affecting Lupus I, it is likely doing so through the momentum flux of its expansion. This transfer of momentum could be causing

the velocity gradient across the B 228 ridge (in the direction of the H I shell's expansion); this process could be analogous to the 'streamers' in the Ophiuchus complex (de Geus 1992). The enhanced linewidth at the NW end of B 228 and along the leading edge of the ridge (implying increased pressure in the molecular gas) is also consistent with the effect of the H I shell. More detailed studies of both H I and molecular gas may support the idea of Lupus I being affected by the Upper-Sco shell: Better estimates of the volume density of H_2 and higher-resolution maps of H I are required.

5.4. Lupus III

The brightest part of Lupus III near HR 5999 and 6000 was mapped by Tachihara et al. (2007) in the mm-wave continuum, $C^{18}O$ 1–0 and $H^{13}CO^+$ 1–0, all with higher resolution than the AST/RO data. The $C^{18}O$ emission peak coincides with the CO peak in our maps, and extends to the east, with another E–W elongation a few arcminutes to the north. The continuum map, together with a near-IR extinction map (Nakajima et al. 2000), shows the same southern E–W structure extending further east, while the northern structure breaks up into two clumps, the denser western one containing a Class 0 protostar (Lupus 3 MMS). In the $H^{13}CO^+$ map, there is no emission at the CO peak; the emission peaks strongly to the east in the southern E–W structure, while the clumps in the northern structure show up as smaller peaks.

Tachihara et al. (2007) suggest that the lack of $H^{13}CO^+$ emission at the CO peak can be accounted for by a long path length through gas with volume density significantly lower than the critical density ($\sim 10^5\,\mathrm{cm}^{-3}$ for $H^{13}CO^+$). They estimate a column density of $1.2 \times 10^{22}\,\mathrm{cm}^{-2}$, equivalent to A_V of about 13 mag, which is consistent with the extinction maps (Chapman et al. 2007). The peak T_R^* in CO 4–3 (about 9 K) implies $T_x \gtrsim 18$ K, while the 6 K peak T_R^* of ^{13}CO 2–1 only requires $T_x \gtrsim 11$ K. Compared to the rest of the Lupus clouds, where the CO 4–3 and ^{13}CO 2–1 excitation temperatures are quite similar, this is a significant discrepancy. It could be explained by the CO peak being compact, as suggested by the CO 4–3 peak T_R^* map, so that the ^{13}CO 2–1 measurement is beam-diluted. Alternatively, the CO 4–3 could be tracing an outer shell heated by the HAe/Be stars. However, the ^{13}CO 2–1 emission is also optically-thick (for $T_x = 11$ K, A_V of 13 mag implies an optical depth of about 8), and so will trace similar material. These temperature estimates tend to support the argument that the gas is too warm for depletion of $H^{13}CO^+$ to explain the lack of emission towards the CO peak (Tachihara et al. 2007), although the estimates are unlikely to apply to the centre of the clump. The strong CO 4–3 emission implies that the transition is thermalised, so a significant amount of the gas in the clump must have volume

density $\gtrsim 3 \times 10^4\,\mathrm{cm}^{-3}$. While Tachihara et al. (2007) derived an average volume density of $10^4\,\mathrm{cm}^{-3}$, there must be enough significantly denser gas to thermalise the CO 4–3 line, but not enough to excite the $\mathrm{H^{13}CO^+}$ 1–0 transition.

In projection, Lupus III lies far away from any part of Sco-Cen (Tachihara et al. 2001), in contrast to Lupus I and Lupus IV (discussed below), so the HAe/Be stars probably influence it far more than the OB associations. However, there is evidence for Lupus III being further away than Lupus I and IV, possibly as much as 50 pc (e.g. Comerón 2008). If this is the case, then Lupus III could lie behind Sco-Cen, and be could affected by either or both of Upper-Sco and Upper-Cen-Lup. The large linewidths seen towards Lupus III N could be caused by external influence in the same way as the broader lines seen towards Lupus I.

5.5. Lupus IV

The peak T_R^* in CO 4–3 towards Lupus IV of about 4 K, implying $T_x \gtrsim 12$ K, occurs around the outside of the extinction peaks, which have peak T_R^* around 3 K ($T_x \gtrsim 10$ K). This suggests that the outside of the clump is significantly externally heated. The ^{13}CO 2–1 peak T_R^* implies $T_x \gtrsim 8$ K, but even this measure is unlikely to sample the extinction maxima properly, since it will be dominated by the outer layers of the structure. The CO 4–3 temperature estimates are in line with those seen at the NW end of B 228, where Lupus I seems to be strongly affected by Upper-Sco. Lupus IV is on the opposite side of the Lupus complex to Lupus I, Upper-Sco and its H I shell (Tachihara et al. 2001), but faces the Upper-Cen-Lup subgroup, which lies to the W and SW. Moreira & Yun (2002) suggested that Lupus IV was shaped by the influences of both subgroups, and noted that some of the velocity gradients they saw in Lupus IV were along the vector towards Upper-Cen-Lup. Much of the enhancement in the peak CO 4–3 T_R^* lies on the S and W sides of the extinction peaks, which is consistent with a picture of external heating by the radiation field from Upper-Cen-Lup. There is, however, no nearby H I shell, the Upper-Cen-Lup shell having passed the Lupus clouds long ago (Moreira & Yun 2002). If interaction with the H I shell causes the enhanced linewidth at the NW end of B 228, the lack of any such interaction in Lupus IV would be consistent with its rather low linewidths.

6. Conclusions

Fully-sampled degree-scale maps of the ^{13}CO 2–1 emission towards the Lupus I, III and IV clouds trace the column density and temperature of the gas, the transition becoming

optically-thick in the cloud cores. The peak T_R^* is well correlated with the near-IR extinction (Chapman et al. 2007; Evans et al. 2007), and a comparison of the two suggests that the bulk of the molecular gas in Lupus has a temperature of 8–10 K, rather than the 10–17 K generally adopted elsewhere (e.g. Tachihara et al. 1996; Moreira & Yun 2002; Teixeira et al. 2005). This estimate is fairly robust to changes in the relationship between ^{13}CO column density and A_V. Estimates of the cloud masses from the ^{13}CO maps are reasonably consistent with those derived from extinction mapping. The differences between these estimates vary greatly from cloud to cloud, and suggest that there may be significant spatial variation in the ^{13}CO-to-A_V relationship, as found in the Perseus complex (Goodman et al. 2009). The linewidths of ^{13}CO 2–1 towards the clouds are higher than previous estimates (Evans et al. 2009), around 2 km s^{-1}, with Lupus III N rather broad and Lupus IV rather narrow.

Fully-sampled CO 4–3 maps covering most of Lupus I and small regions of Lupus III and IV trace dense gas: the peak T_R^* generally indicates excitation temperatures quite close to those of ^{13}CO 2–1, and hence that the transition is largely thermalised. This suggests that the volume density $\gtrsim 10^4$ cm^{-3}, although modelling will be required to ascertain the required density. CO 4–3 emission is pervasive towards Lupus I (the map of which covers a large area), implying that this dense gas is found either throughout or all around the outside of the cloud, although it may comprise a fairly small fraction of the cloud mass.

The physical conditions of the molecular gas vary along the B 228 ridge in Lupus I. At the NW end the gas has broader lines and probably higher temperature than in the bulk of the cloud; the column density is not particularly high and there is only one Class III YSO. In the centre of the ridge, the dark cloud 338.8+16.5 is associated with recent star formation (Tachihara et al. 1996; Shirley et al. 2000); in this area a coherent velocity gradient of about 1 km s^{-1} pc^{-1} runs across the ridge. The SE end of the ridge is complex, with YSOs, enhanced linewidth and integrated intensity on the NW side, and column density (and possibly temperature) peaking to the SE. The enhanced linewidths and velocity gradient in B 228 are consistent with a dynamical interaction between Lupus I and the H I shell around the Upper-Sco subgroup of Sco-Cen (de Geus 1992; Tachihara et al. 2001).

To the north of Lupus III, the small cloud Lupus III N has similar characteristics to the bulk of the other clouds, albeit with broader lines and significant velocity structure. Lupus III itself contains a compact CO peak which is probably heated by the nearby HAe/Be stars HR 5999 and 6000. The gas in this clump contains sufficiently dense gas to thermalise the CO 4–3 transition ($n_c \sim 3 \times 10^4$ cm^{-3}), but not to thermalise the H^{13}CO$^+$ transition mapped by Tachihara et al. (2007), which would require $n \gtrsim 10^5$ cm^{-3}. The rest of Lupus III seems to have quite similar physical conditions to those in the rest of the clouds, and shows no particular sign of being affected by the nearby OB subgroups.

Lupus IV contains peaks of very high column density (Chapman et al. 2007) associated with slightly warmer gas temperatures (10–12 K). These temperatures are estimated from the optically-thick CO 4–3 transition, which is strongest around the extinction cores, suggesting significant external heating. The average linewidth of ^{13}CO 2–1, however, is significantly lower than those of Lupus I and III. Lupus IV faces the Upper-Cen-Lup subgroup of Sco-Cen and Moreira & Yun (2002) suggested that it is influenced by the OB stars; the Upper-Cen-Lup H I shell passed by the Lupus clouds a few Myr ago, so Lupus IV is more likely to be affected by the radiation field from the OB stars.

Despite the basic similiarities in their physical conditions, the three clouds have significant differences: Lupus I appears to be strongly affected by external thermal and dynamical influences from the nearby Upper-Sco OB association, and does not display widespread star formation. Lupus III shows no sign of external influence — parts of the cloud are heated internally by its own young stars. Lupus III N seems entirely quiescent, yet has a large average linewidth. Lupus IV has the greatest column density and the narrowest average linewidth, has almost no star formation as yet, and may be heated externally by the Upper-Cen-Lup OB association.

A detailed spatial comparison of CO and extinction maps will yield more accurate estimates of the physical conditions of the Lupus clouds, as well as mapping the variation in the ^{13}CO-to-A_V ratio. Mapping of additional CO transitions is crucial to the understanding of the clouds: more optically-thin lines (C^{18}O and even C^{17}O) are particularly important. Maps of the Upper-Sco H I shell with comparable resolution to the Lupus maps are required to look for more definitive signs of interaction between the shell and the molecular clouds. More sophisticated radiative transfer calculations are beyond the scope of this work, but are required to use the CO 4–3 emission as a proper constraint on the physical conditions of the gas, and hence to understand the structure of the Lupus clouds and how they are affected by the local environment.

We thank Neal Evans, Fernando Comerón, Bruno Merín, Eric Mamajek and Tracy Huard for valuable discussions, and the many people who helped get AST/RO ready for the 2005 observing season, particularly Jacob Kooi and Craig Kulesa. Christina Hammock kept the liquid helium flowing through the winter: We thank her, and all the South Pole Station staff, for their work. We thank the anonymous referee, whose comments have improved this work. AST/RO was supported by the National Science Foundation, under NSF OPP ANT-0441756. NFHT was also supported by the University of Exeter DVC (Resources) Discretionary Fund and by the European Commission (grant MIRG-CT-2006-044961). This work has made use of: NASA's Astrophysics Data System; the SIMBAD database operated at CDS, Strasbourg; and the *Skyview* facility at NASA's Goddard Space Flight Center.

Facilities: AST/RO.

A. Frequency Calibration

Because the acousto-optic spectrometer (AOS) backends are analog devices, laser mode-hopping causes shifts in their frequency calibration. A number of such shifts occurred over the 9-month period during which these data were taken.

The fundamental frequency calibration for each spectrometer was obtained once, by connecting a frequency synthesiser to the IF input of the AOS to obtain the AOS channel width and the channel number of a fiducial frequency. The frequency scale thus defined was used for all data in this paper, but some corrections had to be made. The change in channel width caused by a mode-hop is negligible, but the entire spectrum is offset by a few channels.

The frequency shifts were tracked with a number of fiducials. Each AOS includes a comb generator which is usually used to obtain several frequency calibration scans per hour, giving excellent frequency tracking. However, the comb generator failed during 2005, so other frequency standards had to be used. For the CO 4–3 observations, the mesospheric CO 4–3 line is so strong that it can be picked up without a switched measurement. So the 'sky' spectra, used to estimate the sky temperature for calibration, show the line at an antenna velocity close to zero. The mesospheric CO abundance has a strong seasonal variation, and became so weak at the end of the austral winter (around September) that it could no longer be seen in the sky spectra. Finally, repeated spectra were taken towards the compact HII region NGC 3576. This source has velocity structure on the scale of the AST/RO beam, so pointing uncertainties translate into velocity uncertainties. These three fiducials were combined to track the frequency scale. The majority of ^{13}CO 2–1 spectra were corrected by 1–3 $\mathrm{km\,s^{-1}}$, and some were corrected by up to 5 $\mathrm{km\,s^{-1}}$. About 90% of the CO 4–3 spectra were corrected by $< 1\,\mathrm{km\,s^{-1}}$, with the remainder corrected by 3.9 $\mathrm{km\,s^{-1}}$.

Frequency shifts also show up as inconsistencies in the maps. The 4–3 observations showed no obvious inconsistencies, but some shifts had to be applied to the ^{13}CO 2–1 data: Channel maps of Lupus I showed that data taken in 2005 November had a significant uncorrected frequency shift compared to earlier, better-calibrated data. In addition, the long-integration spectrum towards one of the reference positions with significant 2–1 emission was shifted by about half a channel with respect to the map spectra into which it was added. This was not corrected, because the facility for combining spectra in COMB only handles integer-channel shifts, and the effect of the shift is negligible, even in the channel maps.

B. CO Emission

The CO and ^{13}CO data in this work are analysed under the assumption of LTE (i.e. the excitation temperature, T_x, and gas kinetic temperature, T_K, are the same). For the two transitions considered in this work, Equation 14.46 of Rohlfs & Wilson (1996) yields

$$T_x = \frac{22.1}{\ln\left(1 + \frac{22.1}{T_R^*(4-3)}\right)}$$

for CO 4–3 (neglecting the CMB term), and

$$T_x = \frac{10.6}{\ln\left(1 + \frac{10.6}{T_R^*(2-1)+0.21}\right)}$$

for ^{13}CO 2–1. These equations are correct if the transitions are optically-thick, and completely fill the beam; otherwise they underestimate T_x. In Lupus, the gas is cold enough ($T_x \lesssim h\nu/k$) that T_R^* is significantly different from T_x.

The column density in the lower level of the ^{13}CO 2–1 transition is given by

$$N_1^{(13)} = 9.69 \times 10^{14} \frac{1}{1 - \exp(-10.6/T_x)} \int \tau \, dv \, \mathrm{cm}^{-2}$$

and this can be converted to the total column density of ^{13}CO by correcting for the partition function: $N^{(13)}/N_1^{(13)}$ ranges from 2.1 to 2.3 for T_x of 7–10 K.

In LTE, the ratio of ^{13}CO 2–1 to 1–0 emission depends only on temperature. If both transitions are optically-thick, the ratio is simply the ratio of brightness temperatures at different frequencies for a given T_x, and will range from 0.7 (at 7 K) to unity (at high temperature). In the optically-thin case, this ratio is multiplied by the ratio of optical depths, which also depends on T_x via the partition function: This ratio ranges from 1 to 2 between 6 K and 15 K, with a high-temperature limit of 3. The 2–1/1–0 line ratio should therefore range from 0.7 to about 2 in Lupus.

The ratio of ^{13}CO 2–1 optical depth to C^{18}O 1–0 optical depth is just the ratio of ^{13}CO 2–1/1–0 optical depths, multiplied by the ^{13}CO/C^{18}O abundance ratio: The ^{12}C/^{13}C isotope ratio is 62 ± 4 in the local ISM (Langer & Penzias 1993), but the double ratio ^{13}CO/C^{18}O is not as well known. Combining the solar ^{16}O/^{18}O ratio of 500 (Zinner 1996) with the local ISM ^{12}C/^{13}C ratio yields ^{13}CO/C^{18}O ~ 8, but Langer & Penzias (1990) point out that ^{12}C/^{13}C and ^{16}O/^{18}O should track one another, being similarly dependent on star formation history, and so a solar ratio (^{13}CO/C^{18}O ~ 5.5, Myers et al. 1983) may be more appropriate. Thus the ratio of optical depths should fall in the range of 4 to about 16. The ratio of ^{13}CO

2–1 emission to $C^{18}O$ 1–0, however, is complicated by the fact that the $C^{18}O$ transition is likely to be fairly optically-thin, while the ^{13}CO transition will have moderate to high optical depth. This will tend to reduce the ratio: Conditions in Lupus are likely to yield emission ratios as low as 2–4.

Below a critical volume density n_c, LTE fails ($T_x < T_K$). The critical density itself depends on physical conditions: The effective spontaneous emission rate A_{ij} is reduced at high optical depth, yielding a lower n_c, and collisional transition rates are temperature-dependent. In the optically-thin limit, n_c(CO 4–3) varies from 2.9×10^4 cm^{-3} at 40 K to 4.2×10^4 cm^{-3} at 10 K (Jansen 1995); the critical densities of CO 1–0 and 2–1 transitions are a few hundred and a few thousand cm^{-3} (Rohlfs & Wilson 1996).

REFERENCES

Allen, P. R. et al. 2007, ApJ, 655, 1095

Andreazza, C. M. & Vilas-Boas, J. W. S. 1996, A&AS, 116, 21

Bachiller, R. & Cernicharo, J. 1986, A&A, 166, 283

Barnard, E. E. 1927, Catalogue of 349 dark objects in the sky (Chicago: U. Chicago Press)

Bohlin, R. C., Savage, B. D. & Drake, J. F. 1978, ApJ, 224, 132

Bourke, T. L., Hyland, A. R. & Robinson, G. 1995a, MNRAS, 276, 1052

Bourke, T. L., Hyland, A. R., Robinson, G., James, S. D. & Wright, C. M. 1995b, MNRAS, 276, 1067

Cambrésy, L. 1997, A&A, 345, 965

Chapman, N. L., et al. 2007, ApJ, 667, 288

Clemens, D. P., Yun, J. L. & Heyer, M. H. 1991, ApJS, 75, 887

Comerón, F., 2008, in Handbook of Star Forming Regions Vol. 2: The Southern Sky, ed. B. Reipurth (San Francisco: ASP)

Comerón, F., Spezzi, L. & López Marti, B. 2009, A&A, in press

Doty, S. D. & Neufeld, D. A. 1997, ApJ, 489, 122

Evans, N. J., II 1999, ARA&A, 37, 311

Evans, N. J., II, Rawlings, J. M. C, Shirley, Y. L. & Mundy, L. G. 2001, ApJ, 557, 193

Evans, N. J., II et al. 2003, PASP, 115, 965

Evans, N. J., II et al. 2007, Final Delivery of Data from the c2d Legacy Project: IRAC and MIPS (Pasadena: SSC)

Evans, N. J., II et al. 2009, ApJS, 181, 321

Feitzinger, J. V. & Stüwe, J. A. 1984, A&AS, 58, 365

Frerking, M. A., Langer, W. D. & Wilson, R. W. 1982, ApJ, 262, 590

de Geus, E. J. 1992, A&A, 262, 258

Goodman, A. A., Benson, P. J., Fuller, G. A. & Myers, P. C. 1993, ApJ, 406, 528

Goodman, A. A., Pineda, J. E. & Schnee, S. L. 2009, ApJ, in press.

Hara, A. et al, 1999, PASJ, 51, 895

Hartley, M., Manchester, R. N., Smith, R. M., Tritton, S. B. & Goss, W. M. 1986, A&AS, 63, 27

Jansen, D. J. 1995, PhD Thesis, Leiden University

Jenness, T. & Lightfoot, J. F. 2000, Starlink User Note 216, Starlink Project, CLRC, UK

Lada, C. J., Lada, E. A., Clemens, D. P. & Bally, J. 1994, ApJ, 429, 694

Langer, W. D. & Penzias, A. A. 1990, ApJ, 357, 477

Langer, W. D. & Penzias, A. A. 1993, ApJ, 408, 539

Lee, C. W. & Myers, P. C. 1999, ApJS, 123, 233

Lee, C. W., Myers, P. C. & Plume, R. 2004, ApJS, 153, 523

Löhr, A. et al. 2007, ApJS, 171, 478

Lombardi, M., Lada, C. J. & Alves, J. 2008a, A&A, 480, 785

Lombardi, M., Lada, C. J. & Alves, J. 2008b, A&A, 489, 143

Merín, B. et al. 2008, ApJS, 177, 551

Moreira, M. C. & Yun, J. L. 2002, A&A, 381, 628

Murphy, D. C. & Myers, P. C. 1985, ApJ, 298, 818

Murphy, D. C., Cohen, R. & May, J. 1986, A&A, 167, 234

Myers, P. C., Linke, R. A. & Benson, P. J. 1983, ApJ, 264, 517

Nakajima, Y., Tamura, M., Oasa, Y. & Nakajima, T. 2000, AJ, 119, 873

Pineda, J. E., Caselli, P. & Goodman, A. A. 2008, ApJ, 679, 481

Rohlfs, K. & Wilson, T. L. 1996, *Tools of Radio Astronomy, 2nd Ed.* (Berlin: Springer-Verlag)

Sandqvist, Aa. & Lindroos, K. P. 1976, A&A, 53, 179

Schneider, S. & Elmegreen, B. G. 1979, ApJS, 41, 87

Shirley, Y. L., Evans, N. J. II, Rawlings, J. M. C. & Gregersen, E. M. 2000, ApJS, 131, 249

Stark, A. A, et al. 2001, PASP, 113, 567

Tachihara, K., Dobashi, K., Mizuno, A., Ogawa, H. & Fukui, Y. 1996, PASJ, 48, 489

Tachihara, K., Toyoda, S., Onishi, T., Mizuno, A., Fukui, Y. & Neuhäuser, R. 2001, PASJ, 53, 1081

Tachihara, K., Onishi, T., Mizuno, A., Fukui, Y. 2002, A&A, 385, 909

Tachihara, K., et al. 2007, ApJ, 659, 1382

Teixeira, P. S., Lada, C. J. & Alves, J. F. 2005, ApJ, 629, 276

Vilas-Boas, J. W. S., Myers, P. C. & Fuller, G. A. 2000, ApJ, 532, 1038

Walker, C. K. et al. 1992, Int. J. Infrared Millimeter Waves, 13, 785

Zinner, E. 1996 in ASP Conf. Ser. 99, Cosmic Abundances, S. S. Holt & G. Sonneborn eds. (San Francisco, ASP), 147

Zucconi, A., Walmsley, C. M. & Galli, D. 2001, A&A, 376, 650

Table 1. Dark clouds in Lupus

HMSTG[a]	LM[b]	VMF[c]	SL[d]	α_{2000}	δ_{2000}	Ref.	YSO[b]	Other
				Lupus I				
337.9+16.4	3379+164	Lu1	···	15 39 37	–34 46 30	LM	Y	FS342[e]
337.6+16.4	···	···	···	15 38 21	–34 59 17	HMSTG	···	FS341[e]
338.2+16.4	3382+164	Lu4	···	15 40 35	–34 40 19	LM	N	
338.8+16.5	3388+165-2	Lu6	···	15 42 19	–33 50 59	LM	N	B228
	3388+165-3	Lu8	···	15 42 40	–33 52 01	LM	N	B228
	3388+165-4	Lu7	SL 12	15 42 43	–34 09 15	LM	Y	B228
	3388+165-5	B228	···	15 43 01	–34 08 48	LM	Y	B228
	3388+165-6	Lu9	···	15 43 18	–34 13 30	LM	N	B228
338.7+17.5	···	···	···	15 39 01	–33 27 38	HMSTG	···	B228
339.0+15.8	···	Lu12	···	15 45 34	–34 40 53	VMF	···	
339.2+16.1	3392+161-1	Lu10	···	15 44 54	–34 17 33	LM	Y	B228
	3392+161-2	···	···	15 45 12	–34 13 21	LM	N	B228
	3392+161-3	···	···	15 45 15	–34 20 43	LM	N	B228
	3392+161-4	···	SL 13	15 45 29	–34 24 40	LM	N	FS349[e] , B228
···	···	Lu2	···	15 39 56	–34 42 50	VMF	···	
···	···	Lu3	···	15 40 10	–33 40 07	VMF	···	B228
···	···	Lu5	···	15 42 03	–33 46 33	VMF	···	B228
				Lupus III				
340.7+9.7	···	···	···	16 11 53	–38 03 48	HMSTG	···	Lu III N
340.9+9.2	···	···	···	16 13 57	–38 16 40	HMSTG	···	BHR 134[f]
340.6+9.0	···	···	···	16 14 03	–38 39 04	HMSTG	···	
340.2+9.0	3402+90-1	Lu34	···	16 11 23	–39 01 33	LM	PM	
	3402+90-2	Lu36	···	16 11 37	–38 58 21	LM	PM	
	3402+90-3	Lu35	···	16 11 45	–39 01 39	LM	PM	
339.7+9.2	3397+92-1	···	SL 14	16 09 42	–39 09 28	LM	Y	
	3397+92-2	···	···	16 10 07	–39 03 47	LM	Y	

Table 1—Continued

HMSTG[a]	LM[b]	VMF[c]	SL[d]	α_{2000}	δ_{2000}	Ref.	YSO[b]	Other
	3397+92-3	Lu32	···	16 10 23	–39 10 48	LM	Y	
339.4+9.5	3394+95	Lu30	···	16 07 49	–39 12 04	LM	N	
···	···	Lu31	···	16 09 08	–39 03 55	VMF	···	
···	···	Lu33	···	16 10 27	–39 05 18	VMF	···	
				Lupus IV				
336.4+8.2	3364+82-1	Lu23	···	16 00 53	–42 04 08	LM	N	
336.6+7.8	···	···	···	16 02 49	–42 13 41	HMSTG	···	BHR 120[f]
336.7+8.2	3364+82-2	···	···	16 01 26	–41 53 06	LM	N	
336.7+7.8	···	···	···	16 03 15	–42 06 27	HMSTG	···	
336.9+8.3	3369+83	Lu25	SL 7	16 02 31	–41 39 48	LM	N	
336.9+7.8	···	Lu26	···	16 04 10	–42 00 40	VMF	···	
···	···	Lu24	···	16 00 18	–42 03 47	VMF	···	

[a]Hartley et al. (1986)

[b]Lee & Myers (1999)

[c]Vilas-Boas et al. (2000)

[d]Sandqvist & Lindroos (1976)

[e]Feitzinger & Stüwe (1984)

[f]Bourke et al. (1995a)

Table 2. Molecular Clouds in Lupus

Cloud		α_{2000}	δ_{2000}	CO 4–3			^{13}CO 2–1			C^{18}O 1–0[a]			^{13}CO 1–0[b]			C^{18}O 1–0[b]			Notes
Hara	VMF			T_R^*	I	ΔV	T_R^*	I	ΔV	T_R^*	I	ΔV	T_R^*	I	ΔV	T_R^*	I	ΔV	
Lupus I																			
337.6+16.4	···	15 38 29	–35 02 14	···	···	···	2.1	4.4	2.1	0.4	0.7	1.3	···	···	···	···	···	···	
338.7+17.5	···	15 39 17	–33 30 06	2.3	6.2	2.8	2.4	6.2	2.6	0.6	0.8	1.6	···	···	···	···	···	···	
337.9+16.5	···	15 39 24	–34 45 39	···	···	···	1.9	3.4	1.8	2.5	1.5	0.6	···	···	···	···	···	···	
338.1+16.7	···	15 39 25	–34 27 33	···	···	···	1.9	2.7	1.4	1.0	0.9	0.9	···	···	···	···	···	···	
···	Lu1	15 39 28	–34 46 22	···	···	···	1.9	3.4	1.8	···	···	···	4.7	3.7	0.8	2.1	1.2	0.5	
···	Lu2	15 39 56	–34 42 50	···	···	···	2.0	3.0	1.5	···	···	···	4.6	3.3	0.7	1.9	1.0	0.5	
···	Lu3	15 40 10	–33 40 07	1.8	4.5	2.5	1.8	3.0	1.6	···	···	···	5.5	9.9	1.7	0.5	0.8	1.6	
338.8+17.2	···	15 40 14	–33 38 41	2.0	5.0	2.5	2.4	5.7	2.4	0.5	0.8	1.3	···	···	···	···	···	···	
···	Lu4	15 40 32	–34 39 40	···	···	···	2.3	5.0	2.2	···	···	···	3.3	2.9	0.8	1.2	0.6	0.5	
···	Lu5	15 42 03	–33 46 33	1.9	4.3	2.2	1.5	4.0	2.7	···	···	···	3.0	4.7	1.5	0.7	0.5	0.7	
···	Lu6	15 42 04	–33 50 36	1.4	2.5	1.8	2.1	5.2	2.4	···	···	···	1.9	1.9	0.9	0.5	0.4	0.8	
···	Lu7	15 42 24	–34 09 02	1.8	3.3	1.8	2.9	5.3	1.9	···	···	···	4.0	3.6	0.9	1.3	1.1	0.8	
···	Lu8	15 42 35	–33 52 50	1.7	4.6	2.7	2.5	6.0	2.4	···	···	···	4.5	6.2	1.3	1.1	0.8	0.7	
338.8+16.5	···	15 42 35	–34 08 58	1.6	2.8	1.8	2.8	7.2	2.6	1.9	2.2	1.2	···	···	···	···	···	···	
339.0+16.7	···	15 42 48	–33 53 56	1.5	4.0	2.7	2.3	6.6	2.8	1.4	1.6	1.1	···	···	···	···	···	···	
···	B228	15 43 02	–34 09 06	1.8	3.3	1.9	3.0	5.2	1.7	···	···	···	5.2	5.9	1.1	0.8	0.8	1.0	
···	Lu9	15 43 10	–34 13 50	1.6	2.3	1.5	2.4	4.4	1.8	···	···	···	4.2	3.6	0.8	0.9	0.4	0.4	
339.1+16.1	···	15 44 59	–34 18 08	2.2	5.8	2.6	3.0	9.1	3.1	1.0	1.5	1.1	···	···	···	···	···	···	
···	Lu10	15 45 06	–34 17 39	2.2	6.3	2.8	2.9	8.6	3.0	···	···	···	3.4	3.3	0.9	0.8	0.5	0.6	
339.1+15.9	···	15 45 30	–34 25 51	3.2	4.9	1.5	2.9	5.9	2.0	2.3	1.5	0.7	···	···	···	···	···	···	
Lupus III																			
···	lu30	16 07 51	–39 11 12	···	···	···	2.4	4.9	2.1	···	···	···	3.2	2.2	0.7	0.3	0.2	0.7	
339.6+9.3	···	16 08 53	–39 06 26	9.0	15.5	1.7	5.6	13.1	2.3	1.9	2.4	1.2	···	···	···	···	···	···	
···	lu31	16 09 08	–39 03 55	4.2	8.0	1.9	3.3	8.0	2.4	···	···	···	1.5	1.8	1.1	0.4	0.2	0.4	
···	lu32	16 10 19	–39 12 16	2.3	3.0	1.3	2.2	5.2	2.3	···	···	···	4.3	3.9	0.9	0.3	0.2	0.7	
···	lu33	16 10 27	–39 05 18	2.5	3.7	1.5	2.1	2.9	1.4	···	···	···	5.1	4.1	0.8	1.2	0.7	0.6	
···	lu34	16 11 16	–39 02 38	···	···	···	0.9	1.9	2.1	···	···	···	1.0	1.0	1.0	0.5	0.2	0.4	
···	lu36	16 11 28	–39 00 21	···	···	···	1.3	3.2	2.5	···	···	···	4.6	3.7	0.8	1.2	0.7	0.5	
···	lu35	16 11 36	–39 04 18	···	···	···	1.4	2.7	2.0	···	···	···	4.4	2.8	0.6	0.6	0.5	0.7	

Table 2—Continued

Cloud		α_{2000}	δ_{2000}	CO 4–3			^{13}CO 2–1			C^{18}O 1–0[a]			^{13}CO 1–0[b]			C^{18}O 1–0[b]			Notes
Hara	VMF			T_R^*	I	ΔV	T_R^*	I	ΔV	T_R^*	I	ΔV	T_R^*	I	ΔV	T_R^*	I	ΔV	
340.7+9.7	···	16 11 58	–38 04 23	1.5	6.0	4.1	2.3	5.4	2.4	0.5	0.9	1.8	···	···	···	···	···	···	Lu III N
							Lupus IV												
···	lu24	16 00 18	–42 03 47	···	···	···	1.4	2.6	1.8	···	···	···	4.1	2.4	0.6	0.8	0.3	0.4	
···	lu23	16 00 57	–42 04 55	···	···	···	1.6	2.9	1.8	···	···	···	4.2	3.8	0.9	1.2	0.7	0.6	
336.4+8.2	···	16 00 57	–42 03 16	···	···	···	2.1	3.7	1.7	2.1	1.4	0.5	···	···	···	···	···	···	
336.7+8.2	···	16 01 46	–41 52 34	3.6	5.4	1.5	3.4	6.5	1.9	2.0	2.0	0.8	···	···	···	···	···	···	
336.9+8.2	···	16 02 34	–41 41 54	2.2	2.9	1.3	2.0	3.7	1.8	1.5	1.3	0.8	···	···	···	···	···	···	
···	lu25	16 02 36	–41 42 26	1.2	1.2	1.0	1.9	3.3	1.7	···	···	···	4.9	2.5	0.5	0.6	0.2	0.4	
336.7+7.8	···	16 03 12	–42 07 43	···	···	···	1.8	3.7	2.0	0.7	0.6	0.9	···	···	···	···	···	···	
336.8+7.9	···	16 03 37	–42 00 55	···	···	···	1.5	3.1	2.1	0.7	0.7	0.8	···	···	···	···	···	···	
···	lu26	16 04 10	–42 00 40	···	···	···	1.4	2.7	1.8	···	···	···	5.2	3.8	0.7	1.1	0.6	0.5	

[a]Hara et al. (1999)

[b]Vilas-Boas et al. (2000)

Table 3. Class 0/I/F YSOs in Lupus

Designation		Class[a]	O/NIR[b]	α_{2000}	δ_{2000}	CO 4–3			^{13}CO 2–1		
SSTc2d[a]	Other					T_R^*	I	ΔV	T_R^*	I	ΔV
				Lupus I							
J154214.6–341026		I	Low	15 42 14.6	–34 10 26	1.8	2.2	1.2	2.5	4.7	1.9
J154301.3–340915	IRAS 15398–3359	0[c]	···	15 43 01.3	–34 09 15	4.3	8.2	1.9	2.8	4.8	1.7
J154506.3–341738		F	Neb	15 45 06.3	–34 17 38	2.1	5.9	2.8	2.9	8.6	3.0
				Lupus III							
J160703.9–391112		F	IR, Old	16 07 03.9	–39 11 12	···	···	···	0.4	0.9	2.4
J160708.6–391407		F	V, Old	16 07 08.6	–39 14 08	···	···	···	0.6	1.8	3.2
J160829.7–390311	Sz102	I	Note	16 08 29.7	–39 03 11	2.6	3.4	1.3	2.7	6.1	2.2
J160831.1–385600		F	···	16 08 31.1	–38 56 00	0.6	1.1	1.7	0.3	0.2	0.8
J160846.8–390207		I	···	16 08 46.8	–39 02 07	4.2	7.8	1.9	2.7	6.0	2.3
J160918.1–390453	Lupus3 MMS	0[c]	Neb	16 09 18.1	–39 04 53	3.5	6.2	1.8	3.3	8.0	2.4
J160934.2–391513		F	···	16 09 34.2	–39 15 13	2.3	4.1	1.8	1.7	3.8	2.2
J161013.1–384617		F	IR, Old	16 10 13.1	–38 46 17	···	···	···	0.4	0.6	1.4
J161027.4–390230		F	Low	16 10 27.4	–39 02 30	2.6	4.4	1.7	1.9	4.5	2.4
J161204.5–380959		F	V, Low	16 12 04.5	–38 09 59	···	···	···	1.2	4.3	3.7
				Lupus IV							
J160115.6–415235		F	Neb	16 01 15.6	–41 52 35	4.5	6.4	1.4	3.6	6.2	1.7

[a]Merín et al. (2008)

[b]From Comerón et al. (2009): Low — below main sequence; Neb — hidden by nebulosity; IR — suspected IR excess; Old — age of order 100 Myr; V — suspected veiling; Note — discussed individually.

[c]see text for details

Table 4. Areas mapped and quality of spectra for both transitions

Region	Area/sq deg	Area/cells	Spectra	Non-linear[a]	% non-linear[a]
		^{13}CO 2–1			
Lupus I	2.57	9258	11856	0	0
Lupus III	1.87	6740	8412	12	0.1
Lupus IV	0.92	3300	3300	0	0
Total					
Lupus	5.36	19298	23568	12	0.05
		CO 4–3			
Lupus I	0.76	10964	12067	939	8
Lupus III N	0.04	625	650	10	2
Lupus III	0.17	2401	3240	150	5
Lupus IV	0.09	1225	1425	15	1
Total					
Lupus	1.06	15215	17382	1114	6

[a]spectra requiring non-linear baseline subtraction

Table 5. Masses and linewidths in Lupus

	Lu I	Lu III N	Lu III	Lu III + Lu III N	Lu IV
$M/M_\odot(A_V \geq 2)$	280^{+150}_{-40}	40^{+50}_{-10}	110^{+80}_{-20}	150^{+120}_{-20}	80^{+70}_{-10}
$M/M_\odot(A_V \geq 3)$	150^{+90}_{-40}	12^{+8}_{-6}	60^{+30}_{-20}	70^{+40}_{-20}	30^{+30}_{-20}
$\overline{\Delta V}/\mathrm{km\,s^{-1}}$	2.3	2.7	2.2	2.4	1.5
rms $\Delta V/\mathrm{km\,s^{-1}}$	0.7	0.9	0.9	0.9	0.4
Previous Work					
$M/M_\odot(^{13}\mathrm{CO}$ 1–0)[a]	880[b]	···	···	220	···
$\Delta V/\mathrm{km\,s^{-1}}(^{13}\mathrm{CO}$ 1–0)[a]	1.9	···	···	1.7	···
$M/M_\odot(^{13}\mathrm{CO}$ 1–0)[c]	···	···	···	···	$\lesssim 150$
$M/M_\odot(\mathrm{C^{18}O}$ 1–0)[d]	240	5	···	80	160
$\Delta V/\mathrm{km\,s^{-1}}(\mathrm{C^{18}O}$ 1–0)[d]	0.6–1.7	1.8	1.2	···	0.5–0.9
$M/M_\odot(A_V \geq 2)$[e]	251	···	···	250[f]	120

[a]Tachihara et al. (1996)

[b]Covering a larger area than the present work; see Section 4.1

[c]Moreira & Yun (2002)

[d]Hara et al. (1999)

[e]Evans et al. (2009) and N. J. Evans II, priv. comm.

[f]assuming a distance of 150 pc

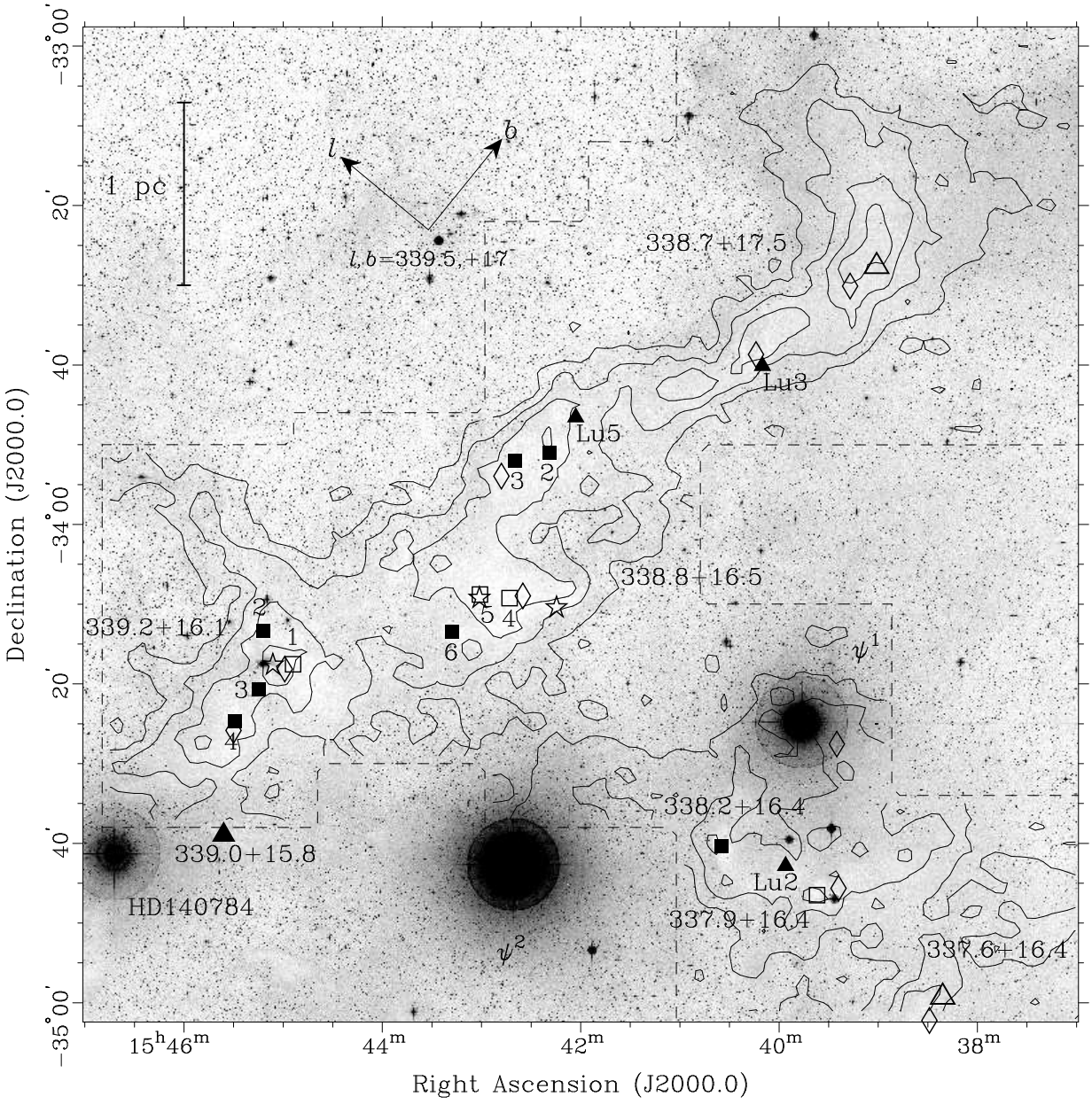

Fig. 1.— Optical (blue DSS2) image of Lupus I, overlaid with ^{13}CO 2–1 emission from this work (contours at 1, 3, 5, 7, 9 K km s^{-1}). Annotations denote: Dark cloud positions (Table 1) from Hartley et al. (1986, open triangles), Vilas-Boas et al. (2000, filled triangles) and Lee & Myers (1999, squares); embedded YSOs from Merín et al. (2008, star-shapes); bright stars (by name); C^{18}O 1–0 peaks from Hara et al. (1999, diamonds). Filled squares denote cloud cores observed in molecular lines by Lee et al. (2004). Only objects within the ^{13}CO map are plotted. The l, b arrows are 15′ long.

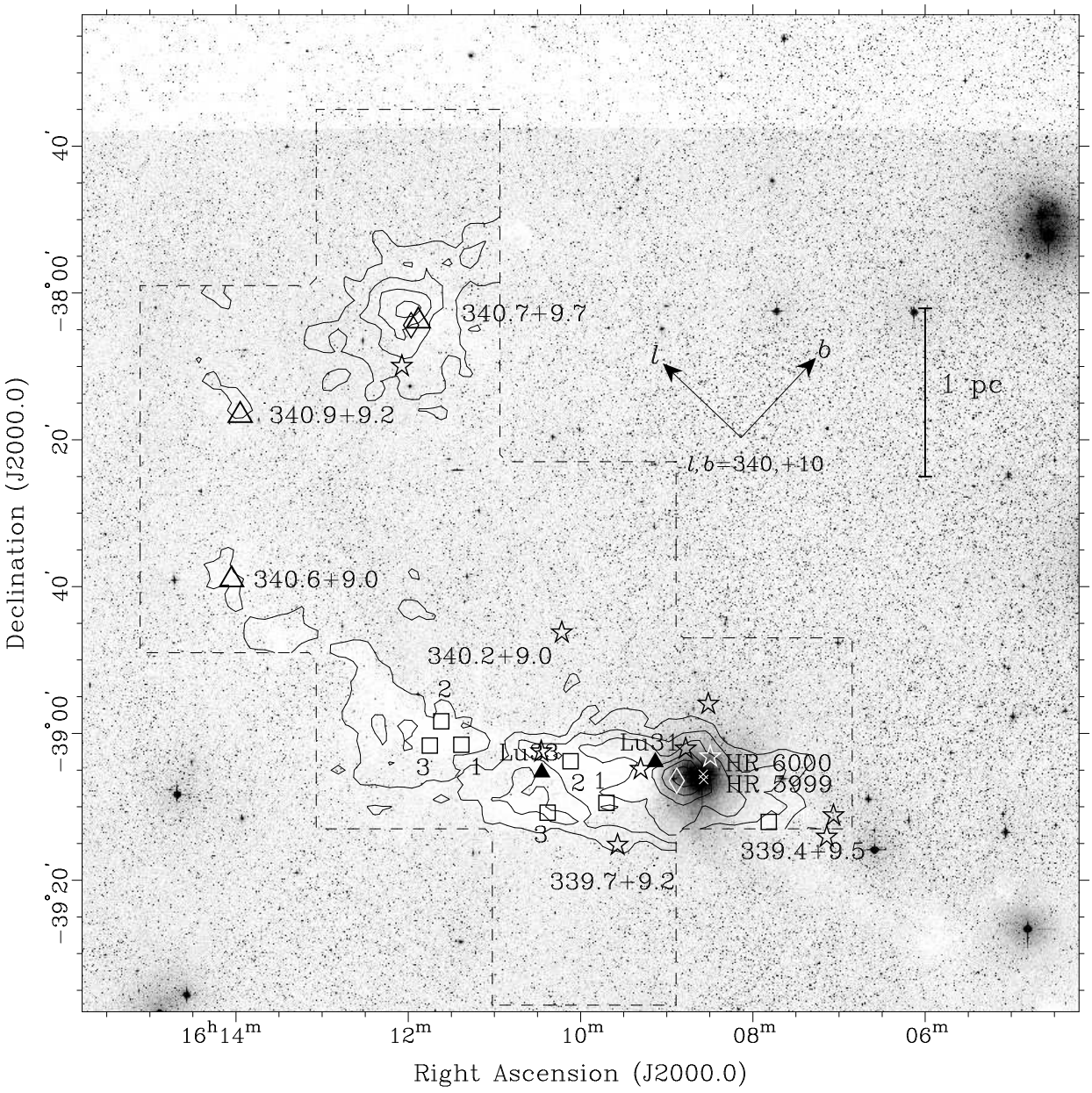

Fig. 2.— Optical image of Lupus III, as in Fig. 1. ^{13}CO contours are at 2, 4, ... 12 K km s^{-1}. Bright stars are marked as crosses.

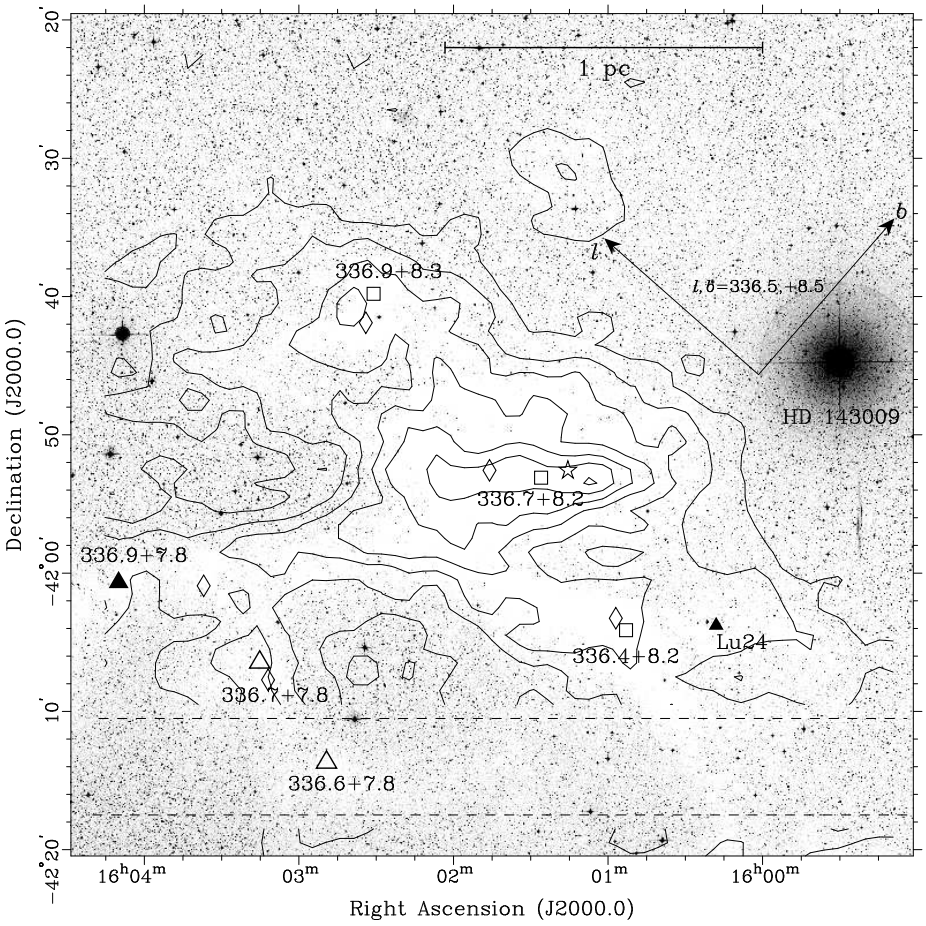

Fig. 3.— Optical image of Lupus IV, as in Fig. 1. ^{13}CO contours are at 1, 2, ... 7 K km s^{-1}.

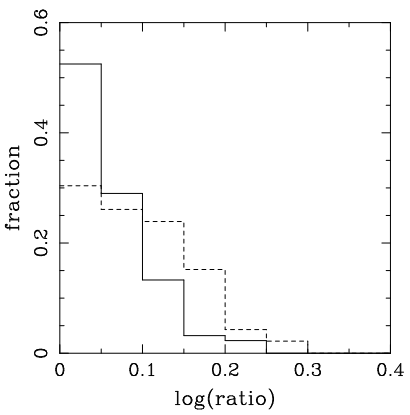

Fig. 4.— Distributions of the logarithms (base 10) of the peak intensity ratios for points with multiple ^{13}CO 2–1 (solid) and CO 4–3 (dashed) spectra, in all maps. Only ratios with estimated S/N>2 are included.

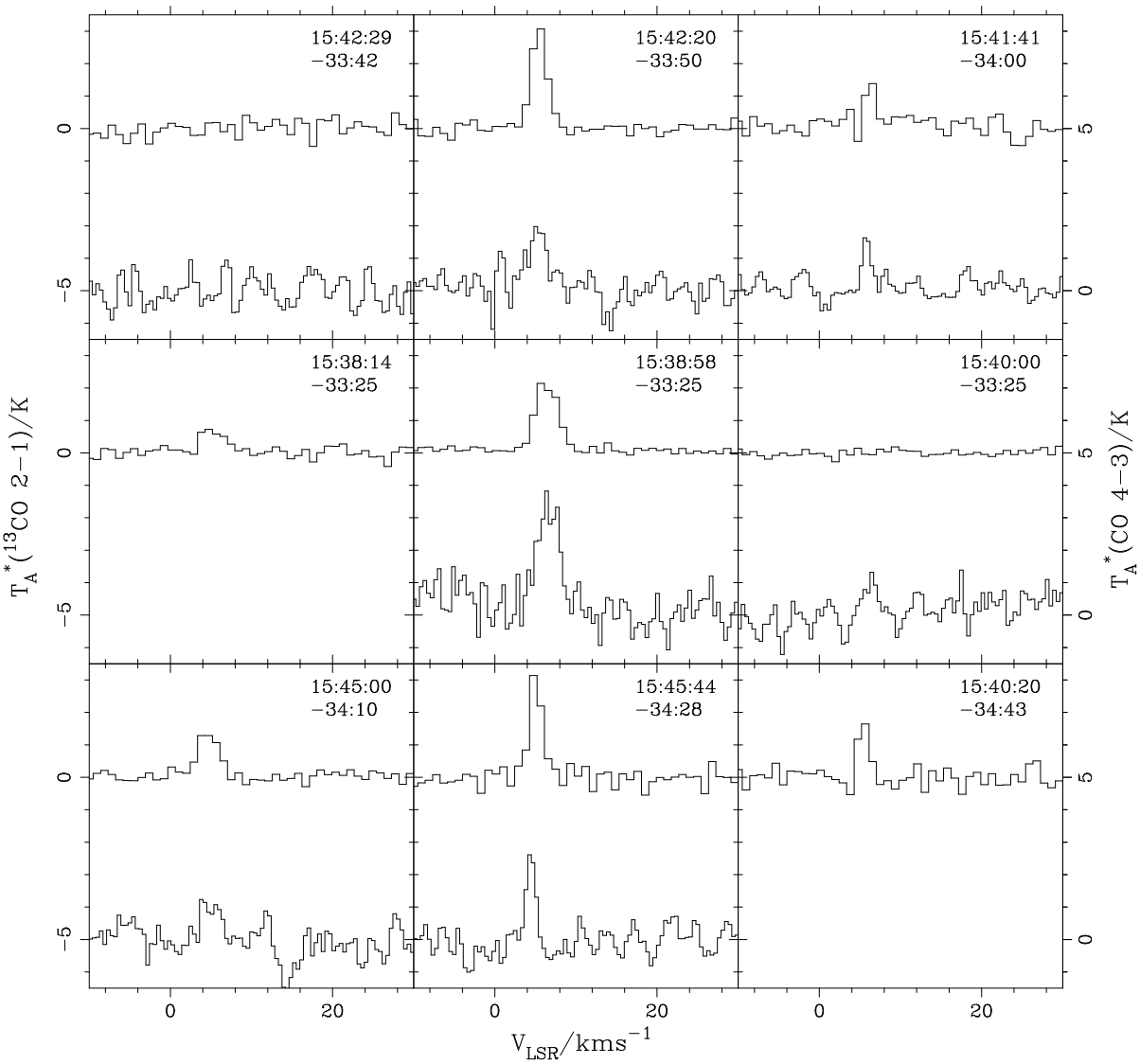

Fig. 5.— Sample spectra towards Lupus I: Each panel shows a ^{13}CO 2–1 spectrum (with position annotated). If there is a CO 4–3 spectrum towards that position (within 0.25′), it is shown below the ^{13}CO 2–1 spectrum.

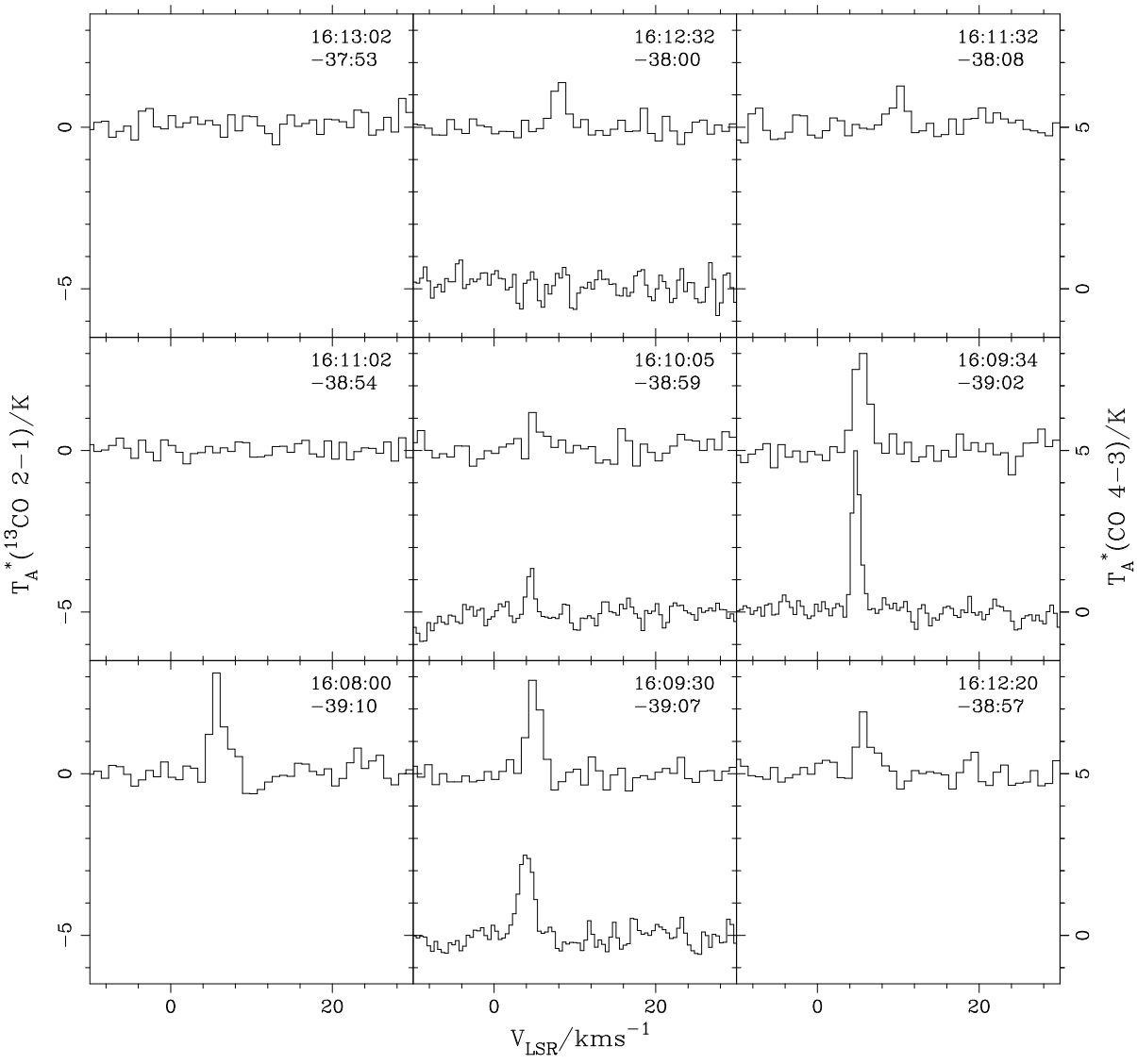

Fig. 6.— Sample spectra towards Lupus III N (upper row) and Lupus III (lower row). See Figure 5 for details.

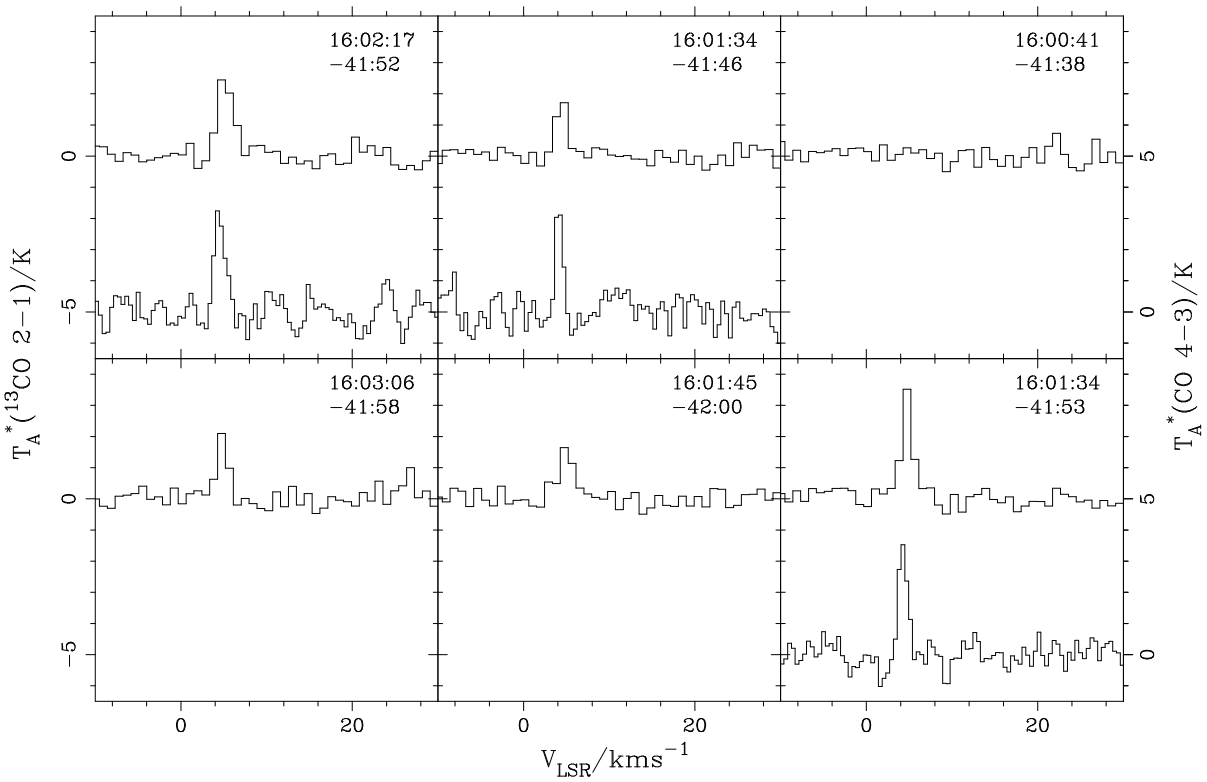

Fig. 7.— Sample spectra towards Lupus IV. See Figure 5 for details.

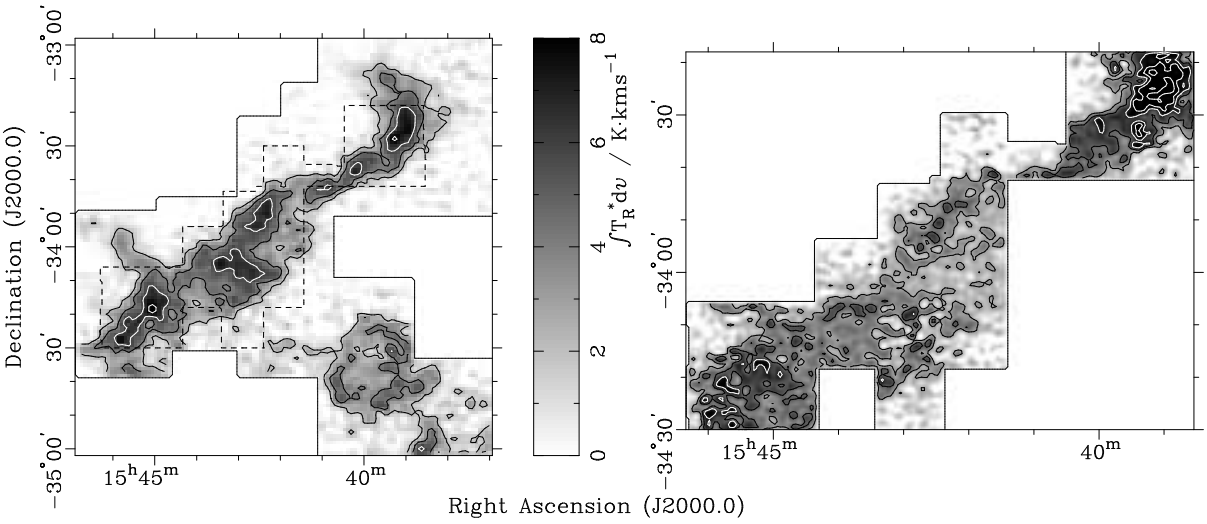

Fig. 8.— Maps of Lupus I in (left) ^{13}CO 2–1 and (right) CO 4–3, integrated from $v_{LSR} = +2$ to $+10\,\mathrm{km\,s^{-1}}$. ^{13}CO 2–1 contours at: 2, 4 K km s^{-1} (black) and 6, 8 K km s^{-1} (white); CO 4–3 contours at: 3, 5 (black) and 7, 9, 11 K km s^{-1} (white). The broken outline denotes the extent of the CO 4–3 map.

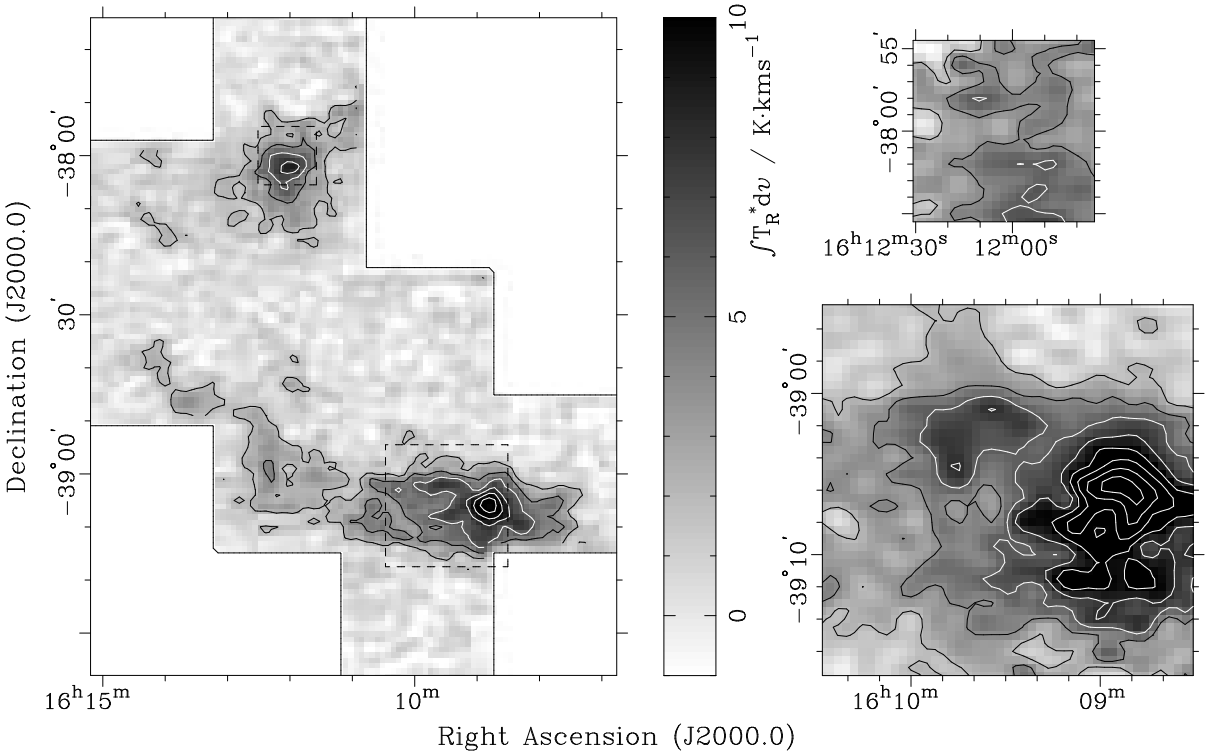

Fig. 9.— Maps of Lupus III and Lupus III N in (left) ^{13}CO 2–1, integrated from $v_{LSR} = +2$ to $+12\,\mathrm{km\,s^{-1}}$, and (right) CO 4–3, integrated from $v_{LSR} = +2$ to $+8\,\mathrm{km\,s^{-1}}$ towards Lupus III and from +6 to $+12\,\mathrm{km\,s^{-1}}$ towards Lupus III N. Contours at: 2, $4\,\mathrm{K\,km\,s^{-1}}$ (black) and 6, $8\ldots16\,\mathrm{K\,km\,s^{-1}}$ (white)

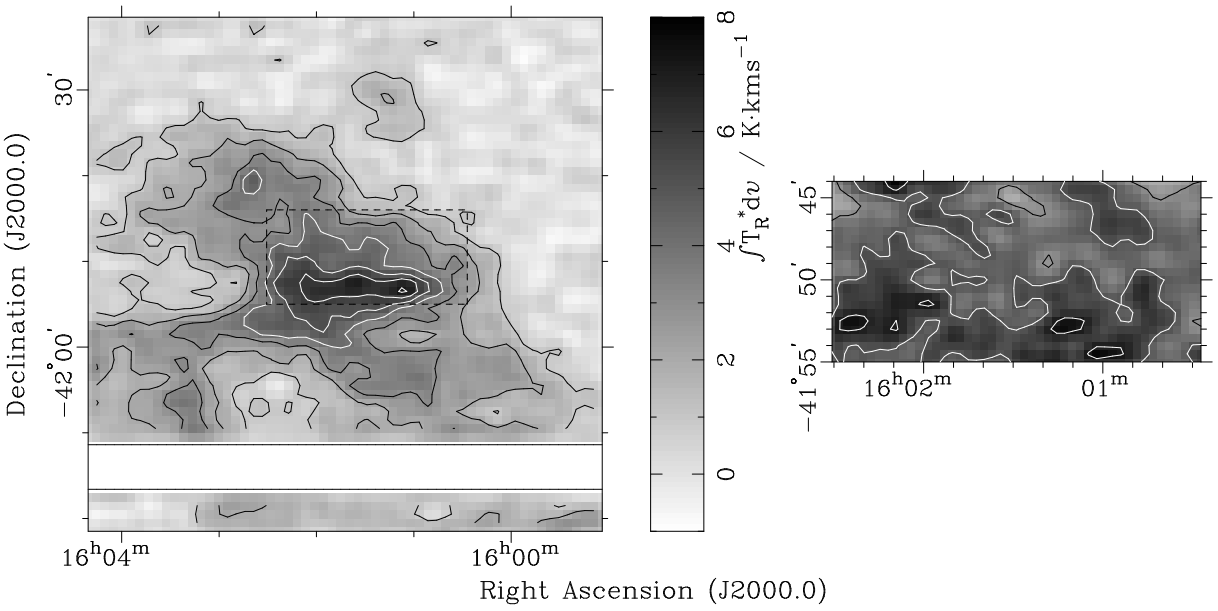

Fig. 10.— Maps of Lupus IV in (left) ^{13}CO 2–1 and (right) CO 4–3, integrated from v_{LSR} = +3 to +7 km s^{-1}. ^{13}CO 2–1 contours at: 1, 2, 3 K km s^{-1} (black) and 4, 5, 6, 7 K km s^{-1} (white); CO 4–3 contours at 3 K km s^{-1} (black) and 5, 7 K km s^{-1} (white).

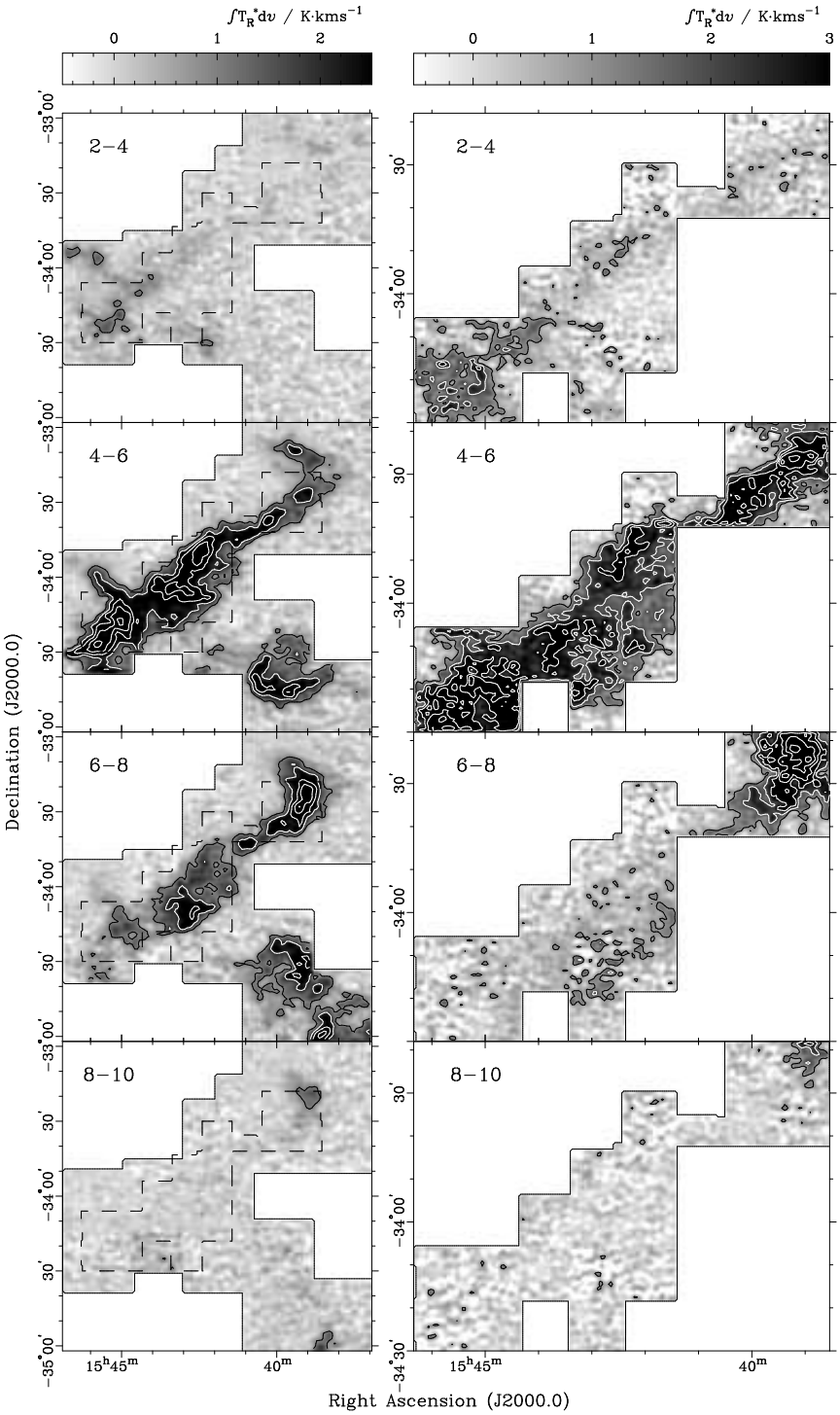

Fig. 11.— Channel maps of Lupus I in (left) ^{13}CO 2–1 and (right) CO 4–3, labelled with v_{LSR} range in km s^{-1}. Contours at 1 K km s^{-1} (black) and 2, 3...6 K km s^{-1} (white). Broken outlines denote the extent of the CO 4–3 map.

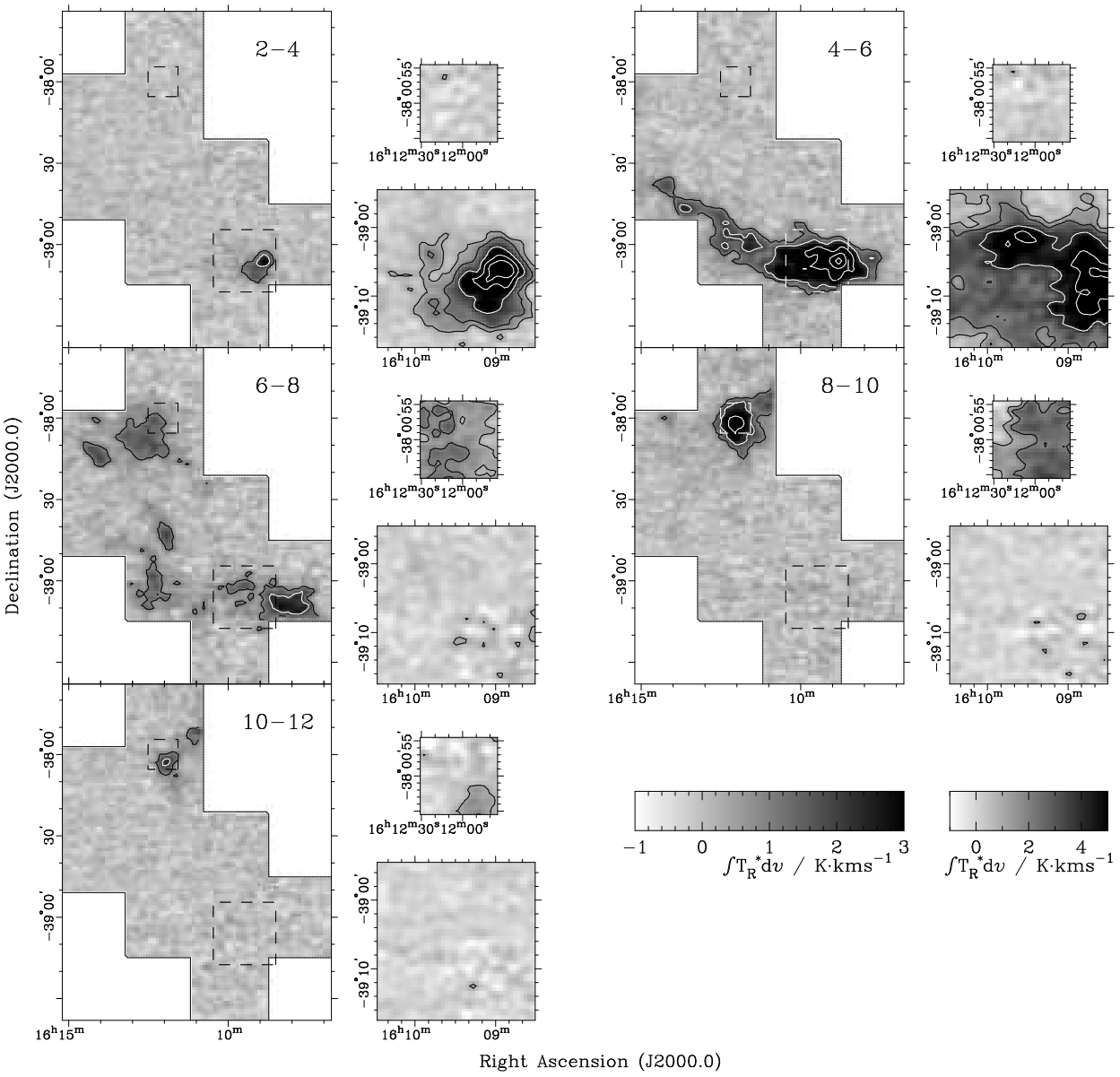

Fig. 12.— Channel maps of Lupus III, as in Fig. 11. ^{13}CO 2–1 contours are at: 1 K km s^{-1} (black) and 2, 4, 6, 8 K km s^{-1} (white); CO 4–3 contours are at: 1, 2 K km s^{-1} (black) and 4, 6, 8 K km s^{-1} (white)

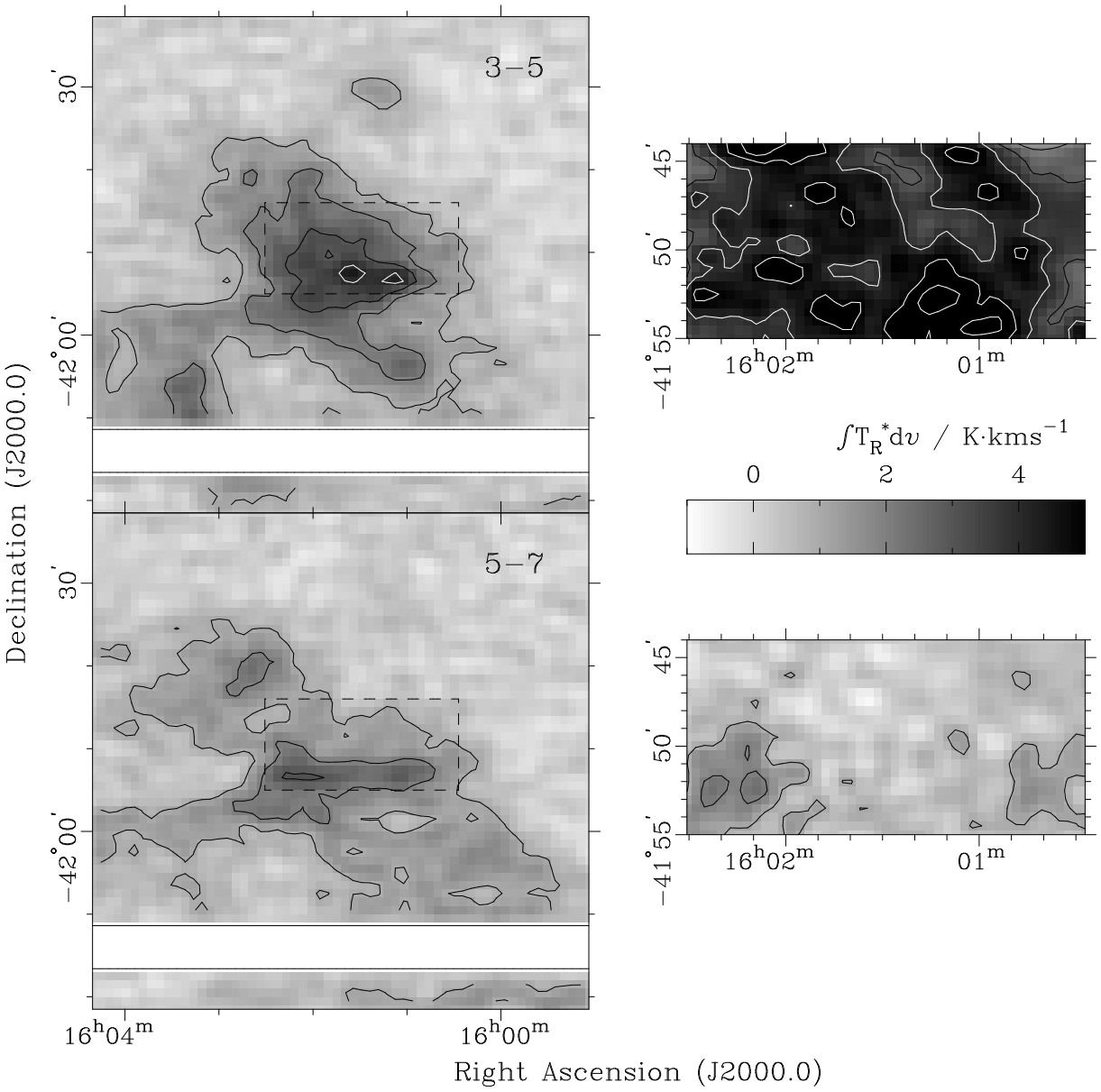

Fig. 13.— Channel maps of Lupus IV, as in Fig. 11. Contours at: 1, 2, 3 K km s^{-1} (black) and 4, 5, 6 K km s^{-1} (white).

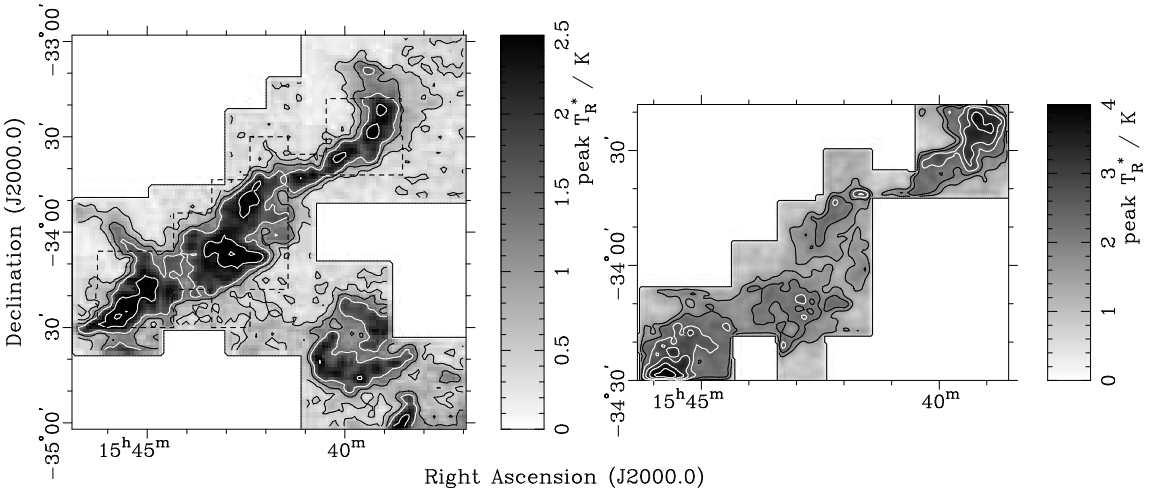

Fig. 14.— Maps of the peak T_R^* of (left) ^{13}CO 2–1 and (right) CO 4–3 towards Lupus I. *Left:* Contours at 0.5, 1 K (black) and 1.5, 2.5, 3.5 K (white). *Right:* Contours at 1.5, 2 K (black) and 2.5, 3, 3.5, 4 K (white). The broken outline denotes the extent of the CO 4–3 map.

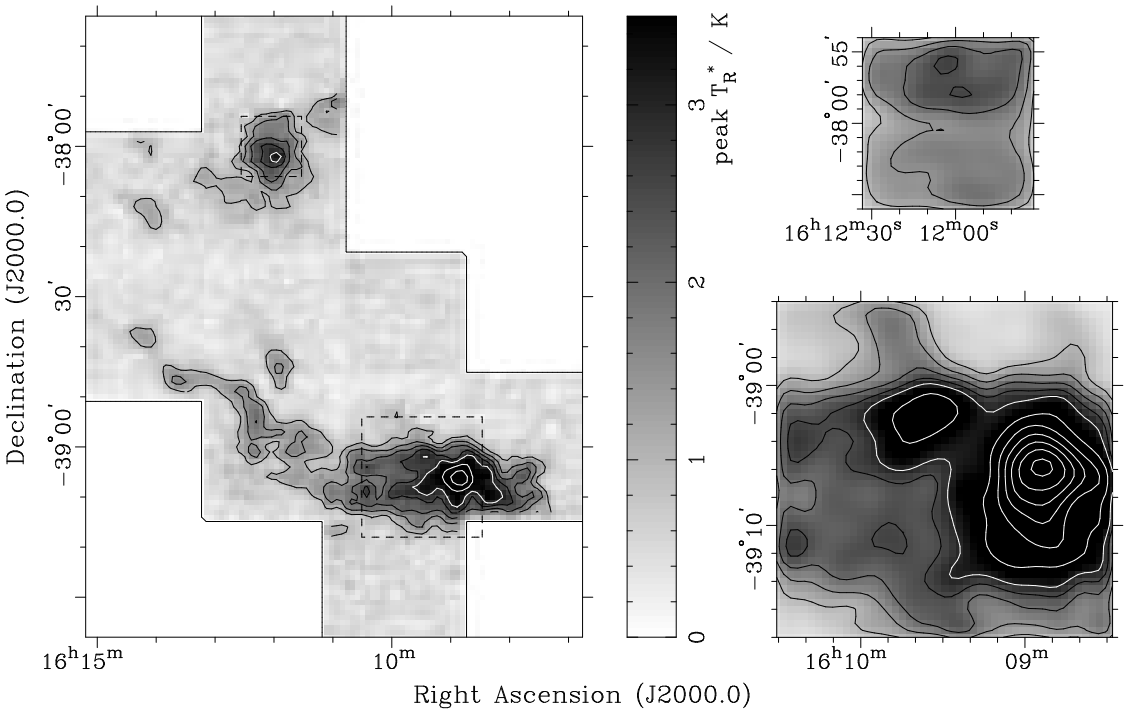

Fig. 15.— Maps of the peak T_R^* towards Lupus III, as in Fig. 14: Contours at 1, 1.5, 2, 2.5 K (black) and 3, 4. . . 9 K (white).

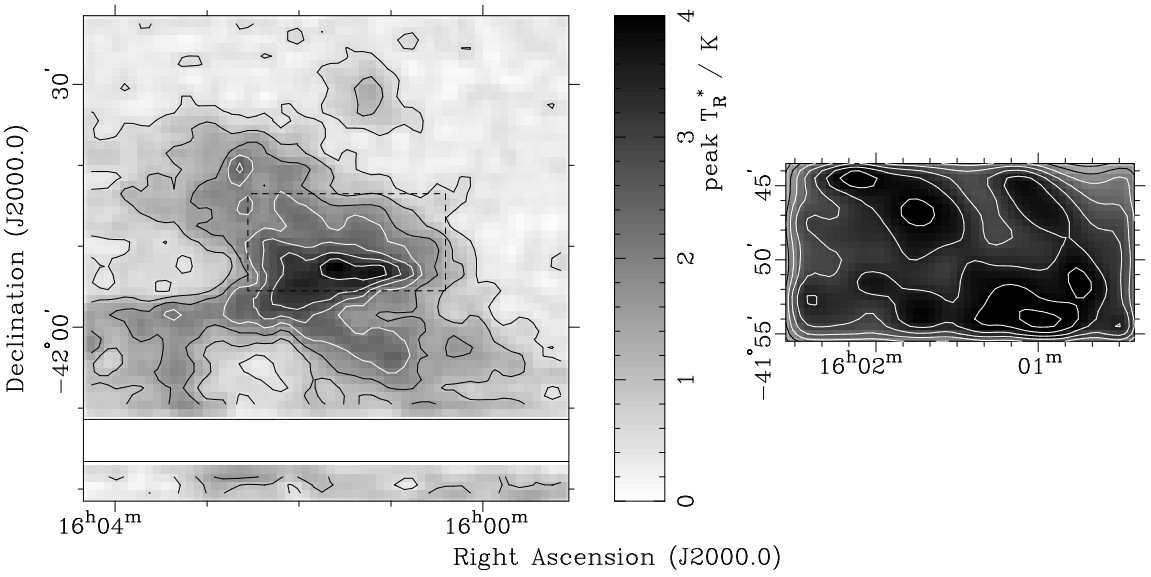

Fig. 16.— Maps of the peak T_R^* towards Lupus IV, as in Fig. 14: Contours at 0.5, 1, 1.5 K (black) and 2, 2.5...4.5 K (white).

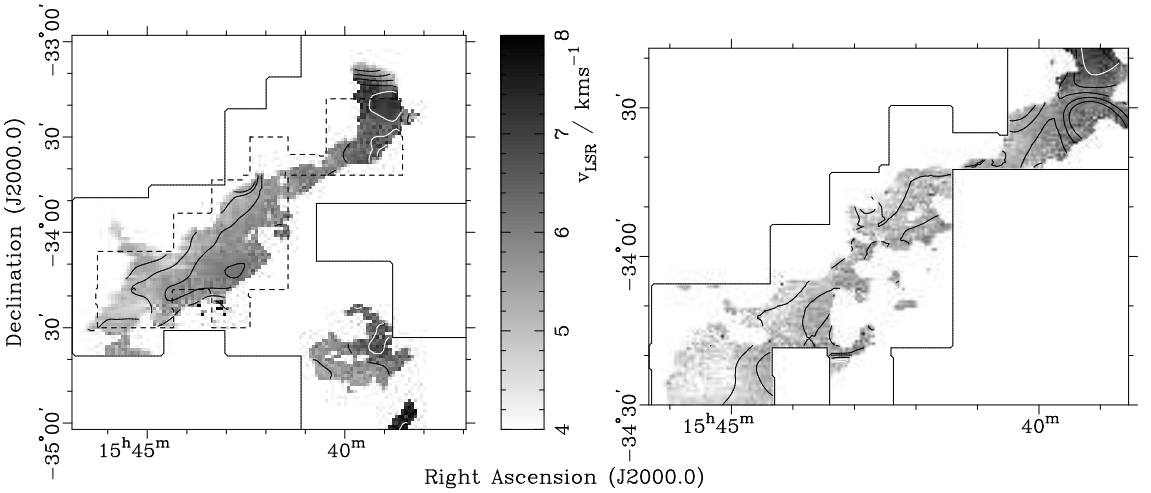

Fig. 17.— Maps of the centroid velocity of (left) ^{13}CO 2–1 and (right) CO 4–3 emission towards Lupus I. Contours are at: 5, 5.5, 6 km s^{-1} (black) and 6.5, 7, 7.5 km s^{-1} (white). The grayscale is unsmoothed, while the contours have been smoothed with a gaussian kernel. Only spectra with S/N>10 are shown. Solid outlines indicate the extent of the maps, while the broken outline indicates the extent of the CO 4–3 map.

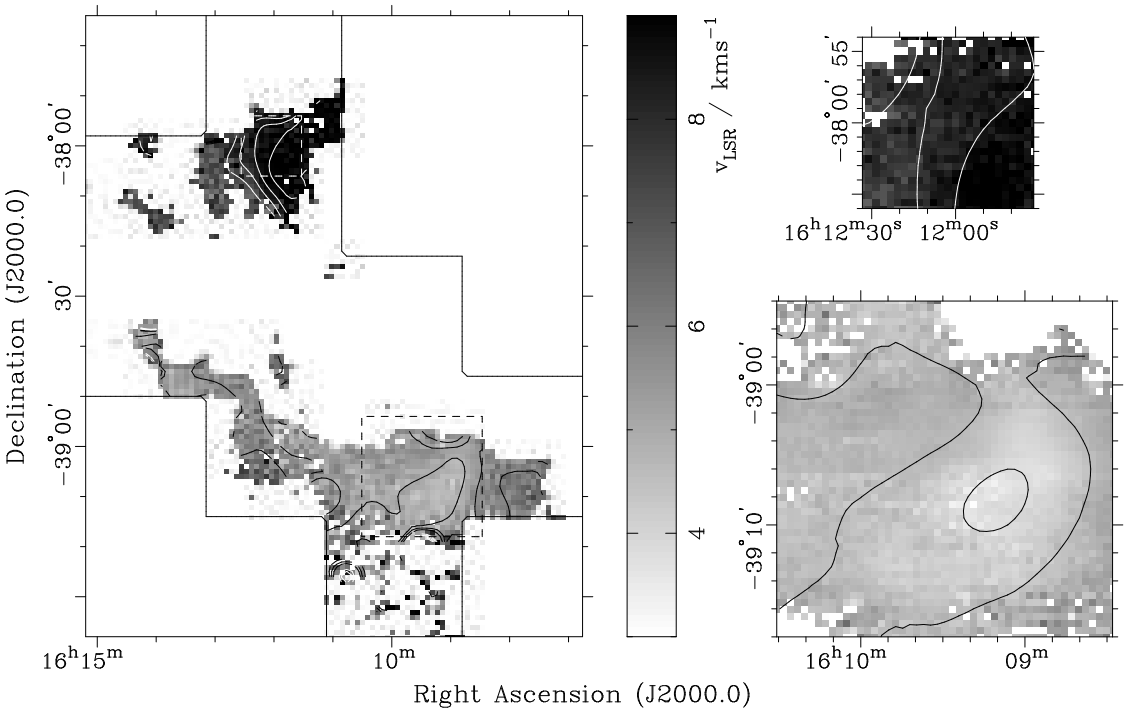

Fig. 18.— Maps of the centroid velocity of emission towards Lupus III, as in Fig. 17: ^{13}CO 2–1 contours are at: 5, 5.5, 6 km s^{-1} (black) and 7.5, 8, 8.5, 9 km s^{-1} (white); CO 4–3 contours are at: 4, 4.5,km s^{-1} (black) and 7.5, 8, 8.5, 9 km s^{-1} (white). Only spectra with S/N>5 are shown.

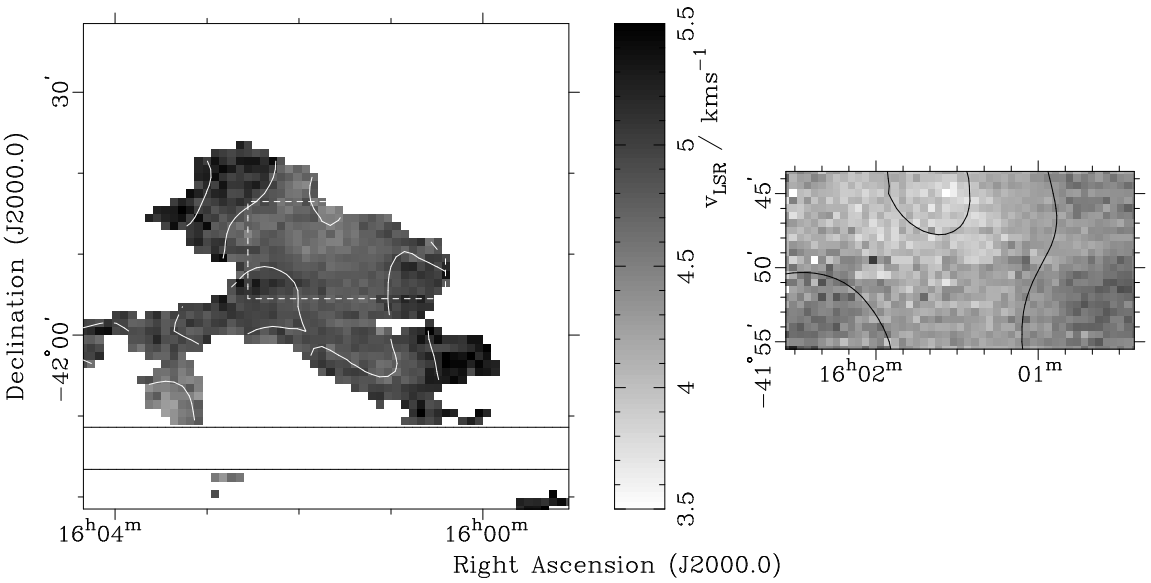

Fig. 19.— Maps of the centroid velocity of emission towards Lupus IV, as in Fig. 17: Contours are at 4, 4.3 (black) and 4.6, 4.9, 5.2 km s^{-1} (white). Only spectra with S/N>10 are shown.

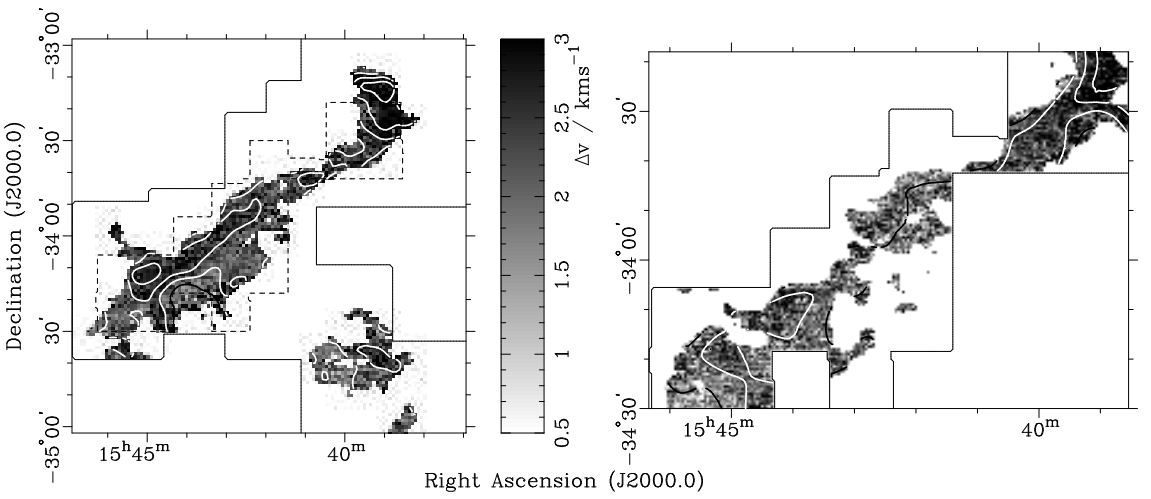

Fig. 20.— Maps of the line widths of (left) ^{13}CO 2–1 and (right) CO 4–3 towards Lupus I. Contours are at: 2, 2.4,... 3.6 km s^{-1}. Grayscale is unsmoothed, while contours have been smoothed with a gaussian kernel. Only spectra with S/N>10 are shown. Solid outlines indicate the extent of the maps, while the broken outline indicates the extent of the CO 4–3 map.

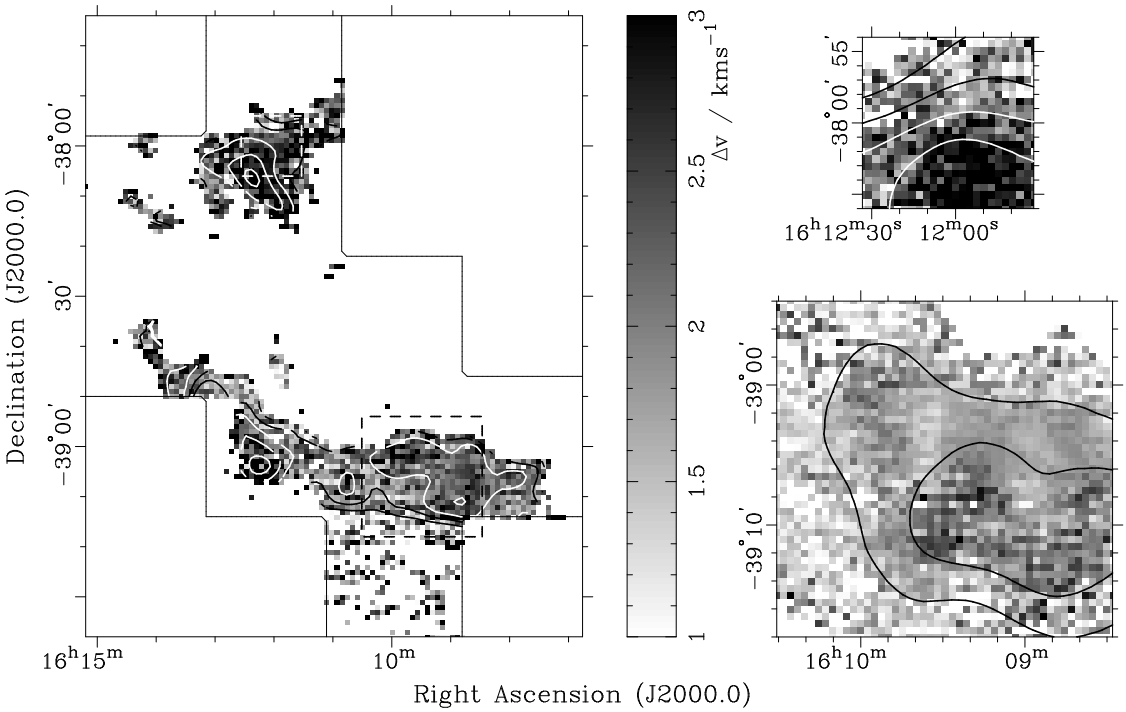

Fig. 21.— Maps of emission line widths towards Lupus III, as in Fig. 20: Contours are at 1.5, 1.8, 2.1 km s^{-1} (black) and 2.4, 2.7, 3 km s^{-1} (white). Only spectra with S/N>5 are shown.

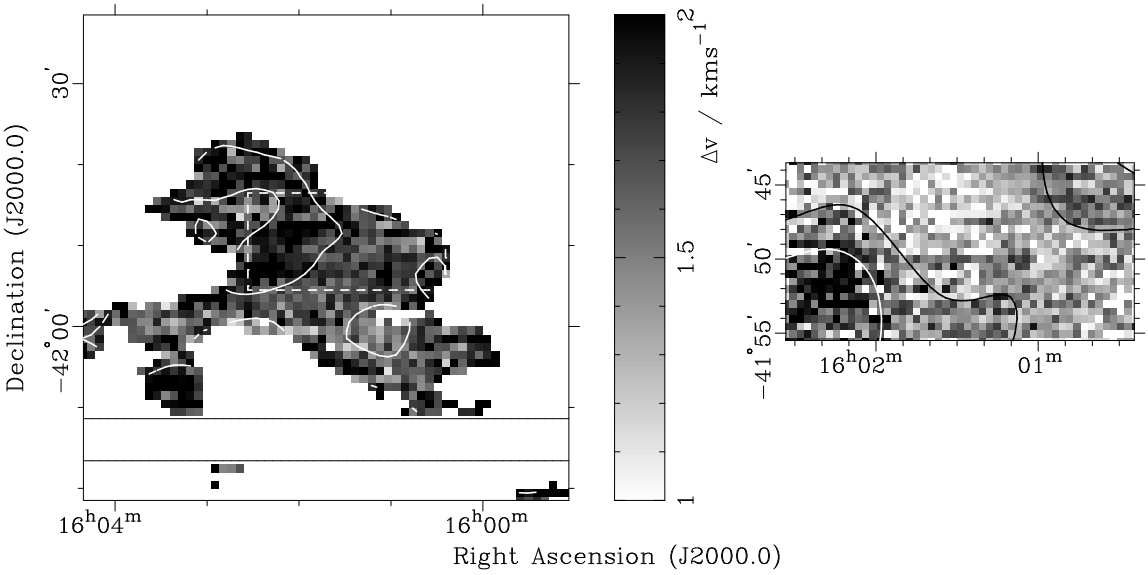

Fig. 22.— Maps of emission line widths towards Lupus IV, as in Fig. 20: Contours at 1.4, 1.6 km s^{-1} (black) and 1.8, 2 km s^{-1} (white). Only spectra with S/N>10 are shown.

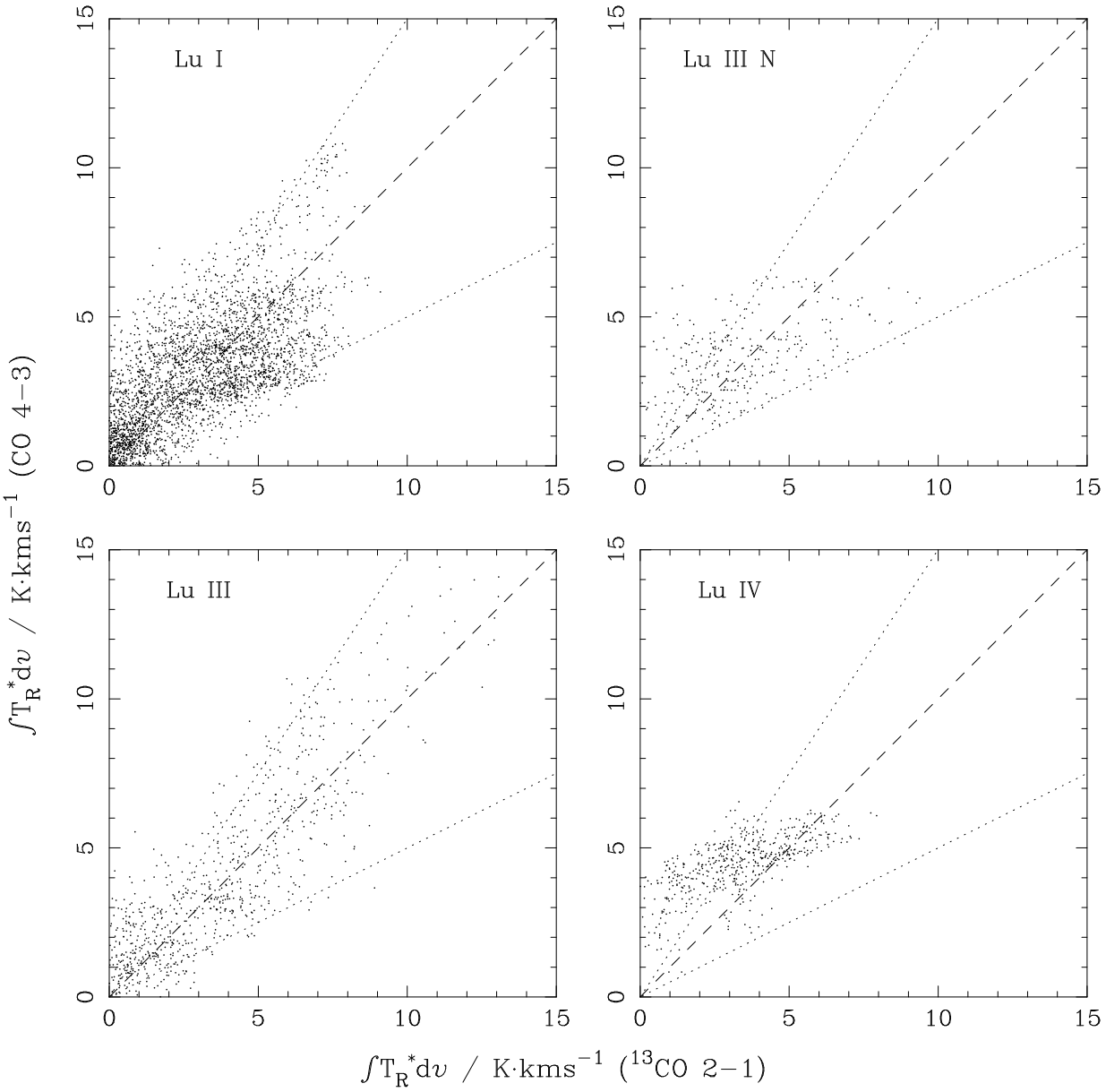

Fig. 23.— Integrated intensities of ^{13}CO 2–1 and CO 4–3 for all regions. The dashed line indicates a ratio of unity, while dotted lines trace ratios (4–3/2–1) of 0.5 and 1.5.

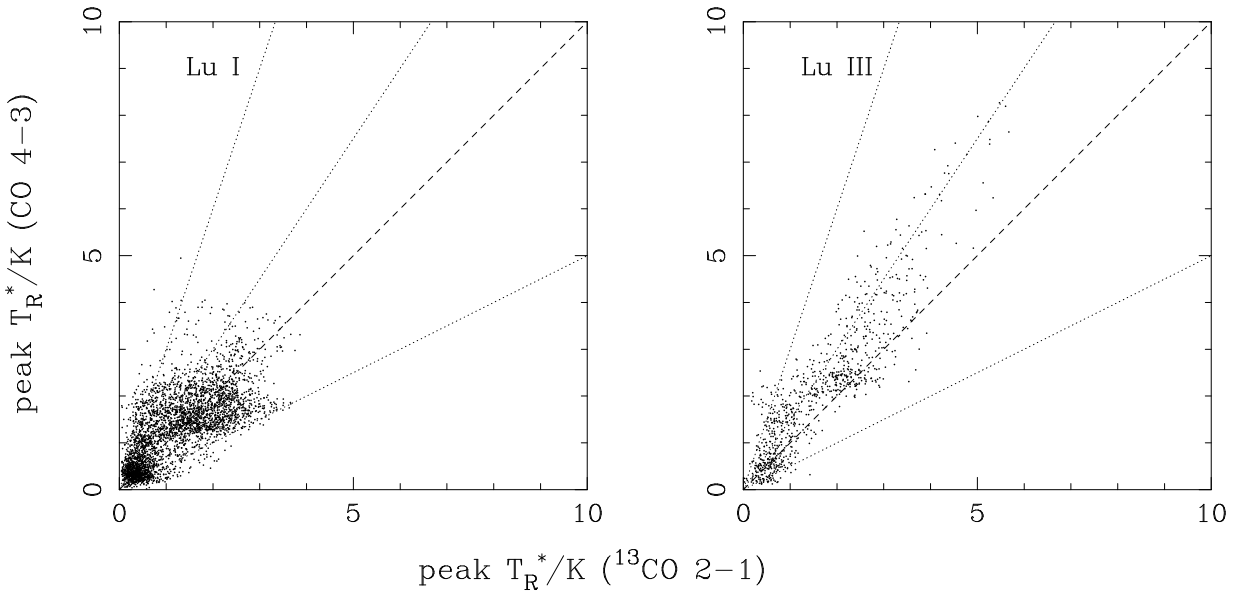

Fig. 24.— Peak T_R^* of ^{13}CO 2–1 and CO 4–3 for Lupus I and III only. The dashed line indicates a ratio of unity, while dotted lines trace ratios (4–3/2–1) of 0.5, 1.5, and 3.

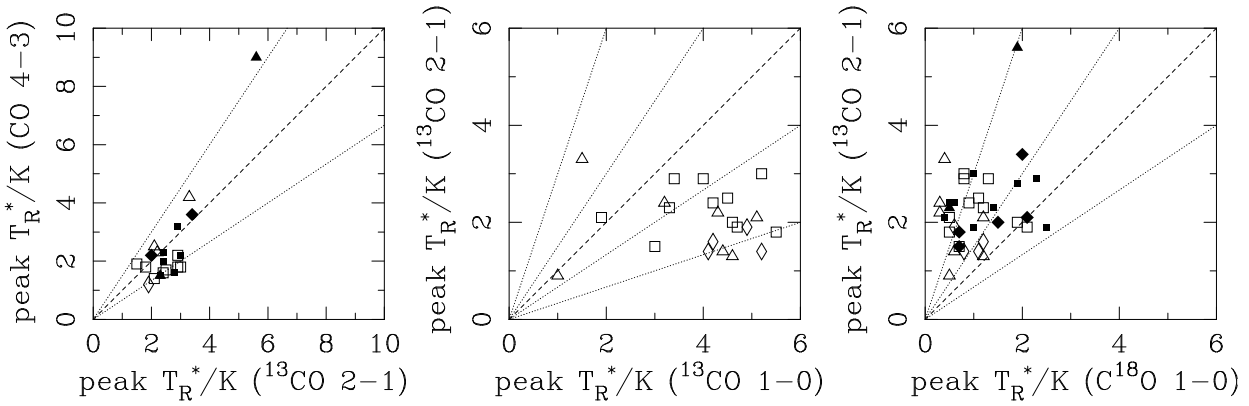

Fig. 25.— Peak T_R^* of CO transitions for cores seen in C^{18}O 1–0. The dashed line indicates a line ratio of unity, while dotted lines trace ratios of 0.67, 1.5 (left), 0.33, 0.67, 1.5, 3 (center), and 0.67, 1.5, 3 (right). Symbols denote cores in Lupus I (squares), Lupus III/III N (triangles), and Lupus IV (diamonds); filled symbols are C^{18}O-selected cores from Hara et al. (1999), and open symbols are extinction-selected cores from Vilas-Boas et al. (2000).

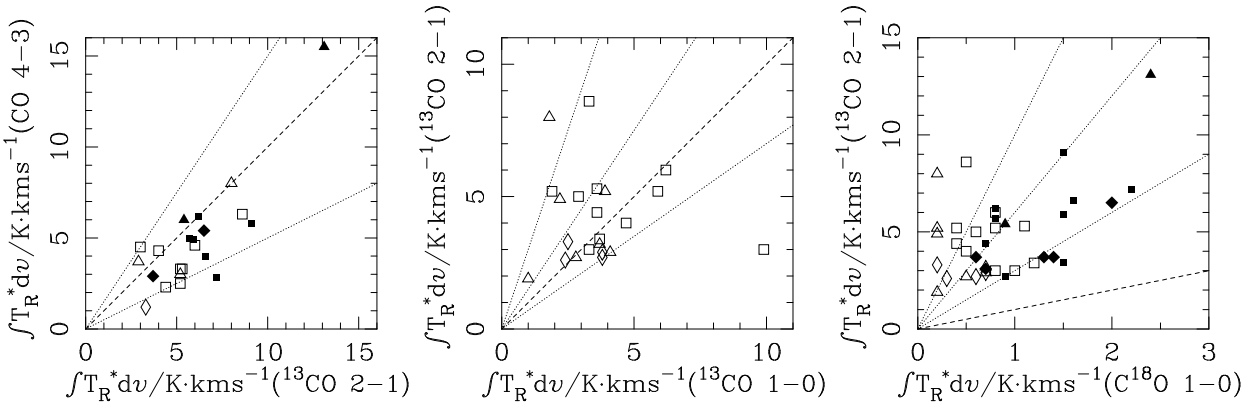

Fig. 26.— Integrated intensities towards $C^{18}O$ cores. The dashed line indicates a ratio of unity, while dotted lines trace ratios of 0.5 and 1.5 (left), 0.67, 1.5, 3 (center), and 3, 6, 10 (right). Symbols are as in Fig. 25.

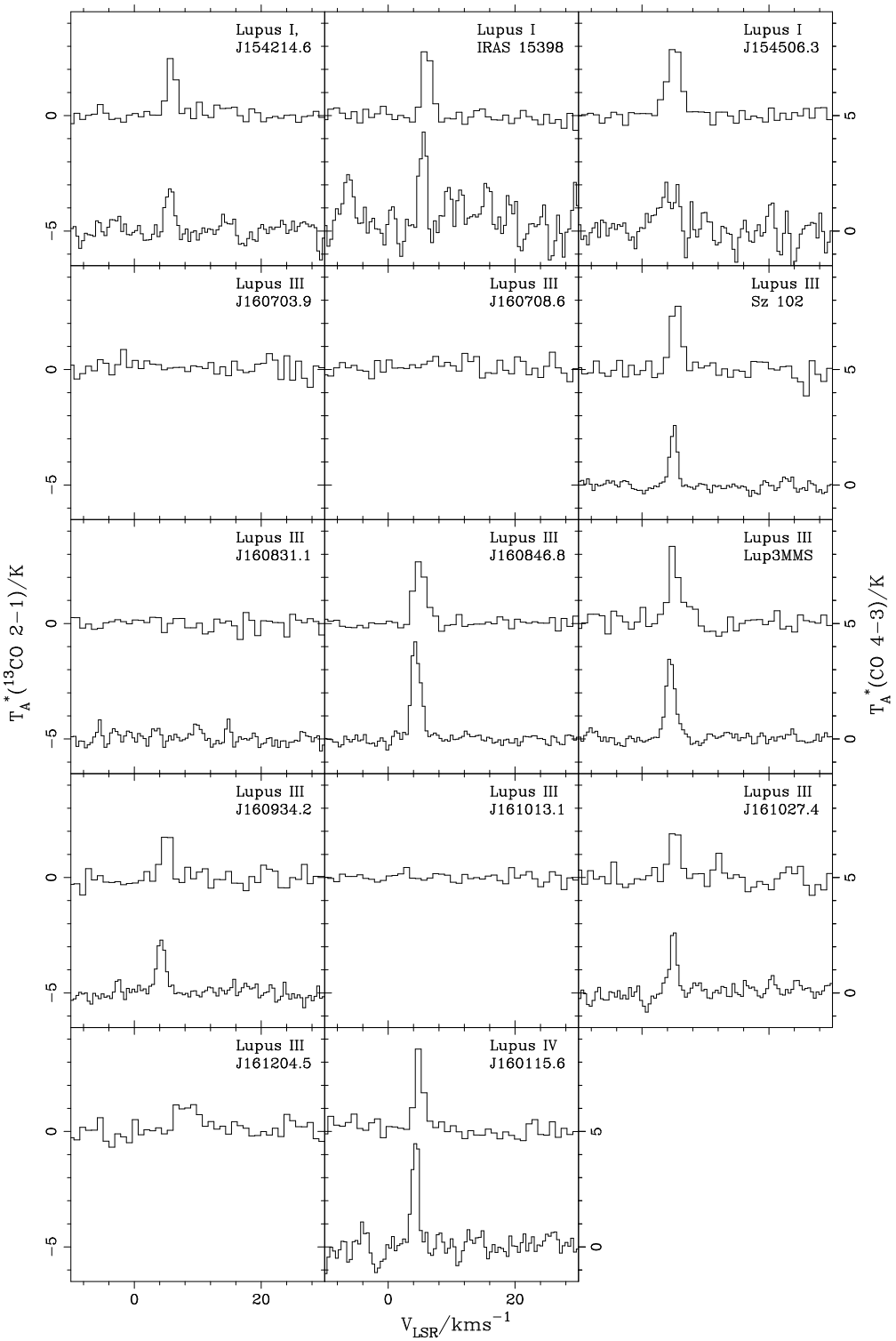

Fig. 27.— Spectra towards the YSOs in Table 3, as for Figs. 5–7.